J. Fluid Mech. (2022), *vol*. 933, A13, doi:10.1017/jfm.2021.1040

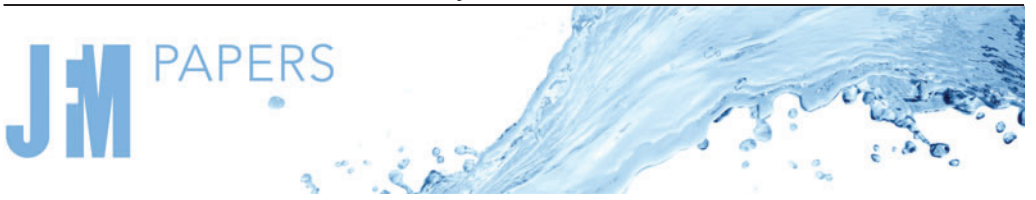

Efficient thrust enhancement by modified pitching motion

Zaka Muhammad[1,2], **Md. Mahbub Alam**[1,†] **and Bernd R. Noack**[3]

[1]Center for Turbulence Control, Harbin Institute of Technology (Shenzhen), University Town, Xili, Shenzhen 518055, PR China

[2]Centres of Excellence in Science and Applied Technologies (CESAT), Islamabad 44000, Pakistan

[3]School of Mechanical Engineering and Automation, Harbin Institute of Technology (Shenzhen), University Town, Xili, Shenzhen 518055, PR China

(Received 17 November 2020; revised 4 October 2021; accepted 21 November 2021)

Thrust and/or efficiency of a pitching foil (mimicking a tail of swimming fish) can be enhanced by tweaking the pitching waveform. The literature, however, show that non-sinusoidal pitching waveforms can enhance either thrust or efficiency but not both simultaneously. With the knowledge and inspiration from nature, we devised and implemented a novel asymmetrical sinusoidal pitching motion that is a combination of two sinusoidal motions having periods T_1 and T_2 for the forward and retract strokes, respectively. The motion is represented by period ratio $\mathbb{T} = T_1/T$, where $T = (T_1 + T_2)/2$, with $\mathbb{T} > 1.00$ giving the forward strokes (from equilibrium to extreme position) slower than the retract strokes (from extreme to equilibrium position) and *vice versa*. The novel pitching motion enhances both thrust and efficiency for $\mathbb{T} > 1.00$. The enhancement results from the resonance between the shear-layer roll up and the increased speed of the foil. Four swimming regimes, namely normal swimming, undesirable, floating and ideal are discussed, based on instantaneous thrust and power. The results from the novel pitching motion display similarities with those from fish locomotion (e.g. fast start, steady swimming and braking). The $\mathbb{T} > 1.00$ motion in the faster stroke has the same characteristics and results as the fast start of prey to escape from a predator while $\mathbb{T} < 1.00$ imitates braking locomotion. While $\mathbb{T} < 1.00$ enhances the wake deflection at high amplitude-based Strouhal numbers ($St_A = fA/U_\infty$, where f and A are the frequency and peak-to-peak amplitude of the pitching, respectively, and U_∞ is the freestream velocity), $\mathbb{T} > 1.00$ improves the wake symmetry, suppressing the wake deflection. The wake characteristics including wake width, jet velocity and vortex structures are presented and connected with $St_d (= fd/U_\infty)$, $A^* (= A/d)$ and $\mathbb{T}$, where d is the maximum thickness of the foil.

Key words: thrust enhancement, efficiency, foil oscillation, modified motion

† Email addresses for correspondence: alam@hit.edu.cn, alamm28@yahoo.com

1. Introduction

Fish have perfected underwater swimming over evolutionary time scales. They have different locomotion depending on body structure and habitat. Theoretical and experimental studies on fish-like propulsion of rigid and flexible foils with simple pitching, heaving and undulatory motions have been studied in the literature. The propulsion efficiency of a rigid foil undergoing pitching or heaving motion is quite low, whereas a high propulsive efficiency can be achieved when both pitching and heaving motions are simultaneously involved (von Kármán & Burgers 1934). The reason for the low thrust and efficiency of a pitching foil, compared with a pitching and heaving foil, is the formation of a relatively narrow jet in the wake. In other words, the proximity of reverse Kármán vortices close to the symmetry line inhibits the thickening of the wake jet (Hanchi *et al.* 2013).

The literature largely focused on the wake structure of rigid pitching propulsors. Depending on the thickness-based pitching Strouhal number St_d $(=fd/U_\infty$, where f is the oscillation frequency, d is the maximum width of the foil and U_∞ is the freestream velocity) and amplitude ratio A^* $(=A/d$, where A is the peak-to-peak amplitude of the pitching), the wake structure of a sinusoidal pitching foil ranges from a simple 2S wake (two single vortices shed in an oscillation cycle) to a complex 8P wake (eight pairs of vortices shed in one oscillation cycle) as observed for thickness-based Reynolds number Re_d $(=\rho U_\infty d/\mu)=220$ and 440 (Schnipper, Andersen & Bohr 2009), where ρ and μ are the density and the dynamic viscosity of the fluid, respectively. The complex wake occurs at $St_d<0.05$ while a 2P + 2S (two pairs and two single vortices shed in an oscillation cycle) or 2P (two pairs of vortices shed per oscillation cycle) wake prevails at $0.05<St_d<0.1$ and a 2S wake persists at $0.1<St_d<0.3$. The 2S Kármán vortex wake is predominant at low A^*, whereas a 2S reverse Kármán wake emerges at high A^* with amplitude-based Strouhal number St_A $(=fA/U_\infty)>0.18$. Two rows of opposite sign vortices (Kármán vortex street) feature in the wake when St_d and/or A^* of a foil is small. An increase in St_d and/or A^* makes the two vortex rows aligned on the wake centreline, which is called a 2S aligned wake. With a further increase in either St_d or A^*, two vortex rows distance from the wake centreline, the vortex rotation signs being opposite to the Kármán vortex street. It is thus known as a reverse Kármán vortex street where the rotation sense of vortices in the two rows produces a jet along the wake centreline. At a high St_d (>0.2) and a high A^* (>1.6), the wake becomes asymmetric, and is deflected away from the wake centreline (see figure 3 of Godoy-Diana, Aider & Wesfreid 2008) at $Re_d=255$. Using stability analysis of pitching NACA0015 foil at $Re_d=255$, Deng, Sun & Shao (2015) showed that the deflection of the wake occurs when the flow transits from two-dimensional (2-D) to three-dimensional (3-D). Moriche, Flores & García-Villalba (2016) conducting 2-D and 3-D simulations of a pitching and plunging NACA0012 foil at chord-based Reynolds number Re_c $(=\rho U_\infty c/\mu)=1000$ found that the near-wake structures obtained from 2-D and 3-D simulations are similar to each other. Additionally, differences in the aerodynamic forces between the 2-D and the 3-D simulations were less than 5 %. Alam & Muhammad (2020) also compared results between 2-D and 3-D simulations at $Re_d=200$ and found that the flow around the oscillating foil at $Re_d=200$ is essentially 2-D. The maximum instantaneous thrust is generated at the instant where the rate of power input changes from positive to negative, i.e. at the inflection point of the power curve. The instantaneous thrust leads the instantaneous power. They analysed the fluid dynamics based on inertia, using relative angular acceleration with respect to the foil showing that the fluid dynamics is strongly dictated by the inertia

of the foil. They mathematically developed a flow model based on Euler, Coriolis and centrifugal accelerations in a non-inertial frame to assimilate the physical insight into the thrust generation and power input. While Euler and Coriolis accelerations were involved in the power input, the centrifugal acceleration was linked to the thrust generation. The normal and reverse Kármán wakes were found to be the attributes of the drag and thrust, respectively, but not the origin of the thrust.

The early experimental studies on pitching foil focused on wake structure and time-averaged forces. The forces were estimated from the momentum balance. It led to an overestimation when unsteady terms (e.g. streamwise velocity fluctuations and pressure) are neglected (Bohl & Koochesfahani 2009). The inclusion of the unsteady terms reasonably predicts the time-averaged forces on high pitching frequency foils whereas under predicts those on low pitching frequency foils (Mackowski & Williamson 2015).

The St_d, A^*, pitching centre and attack angle are all pivotal parameters for thrust generation and efficiency (Triantafyllou *et al.* 2005; Alam & Muhammad 2020). For a given angular amplitude of the foil oscillation, when the pitching centre moves from the leading edge to the foil tip (trailing edge), the amplitude of the foil tail shrinks and hence thrust drops (Tian *et al.* 2016). Interestingly, the experiments of Van Buren *et al.* (2018) showed negligible effects of the free-stream velocity on the wake of a pitching foil at $4770 < Re_c < 9550$ examined. They noted that studies on foil undergoing a constant Re_c could provide robust conclusions of the swimming performance of pitching foils without the need to explore the free-swimming condition. Similarly, a study of a pair of hovering (ascending and descending states) sinusoidal pitching thin foils also indicated that the effect of Re_c is insignificant for Reynolds number larger than 1000 (Zhang *et al.* 2018).

Several studies have reported increased thrust/efficiency of pitching foils with intermittent swimming motion (Videler 1981; Akoz & Moored 2018) or with chord-wise flexibility (Marais *et al.* 2012; Egan, Brownell & Murray 2016; David, Govardhan & Arakeri 2017; Huera-Huarte & Gharib 2017). The waveform of the body motion also affects thrust and efficiency. For example, clapping wings have a lower efficiency than pitching wings (Martin *et al.* 2017) and non-sinusoidal pitching motion enhances thrust or efficiency (Xiao & Liao 2009; Lu, Xie & Zhang 2013; Xie *et al.* 2014; Chao *et al.* 2019). There are two different types of non-sinusoidal motions studied in the literature (figure 1*a*,*b*). The first category is based on shifting the peaks toward (dash–dotted line) or away (solid line) from the midpoint ($t = T/2$, where t is the time and T is the oscillation period) compared with the peaks for the sinusoidal motion (dashed line) (figure 1*a*). A motion trajectory of this category is asymmetric about the peaks but second-order rotational symmetric about point $t = T/2$. It is here termed as a quasi-symmetric waveform. It could be simply described as a faster movement from the lower extreme to the upper extreme than from the upper extreme to the lower extreme (solid line) and *vice versa* (dash–dotted line). The foil undergoing this kind of motion sheds one stronger vortex in the faster stroke and multiple weaker vortices in the slower stroke (Koochesfahani 1989). This motion generates higher thrust and lower efficiency than purely sinusoidal motion (Xiao & Liao 2009). The second category of non-sinusoidal pitching motion is the blend of square and sawtooth waveforms (figure 1*b*). These waveforms are symmetric about the peaks, having the second-order rotational symmetry about the point $t = T/2$, where the change in the blending factor can gradually modify the sinusoidal waveform (dashed line) to a nearly square waveform (dash–dotted line) or to a sawtooth (solid line). The thrust beefs up but the efficiency declines when the sinusoidal waveform is modified to a square waveform. However, the modification of the sinusoidal waveform to a sawtooth waveform cuts down the thrust but enhances the efficiency (Lu *et al.* 2013; Xie *et al.* 2014). A waveform with

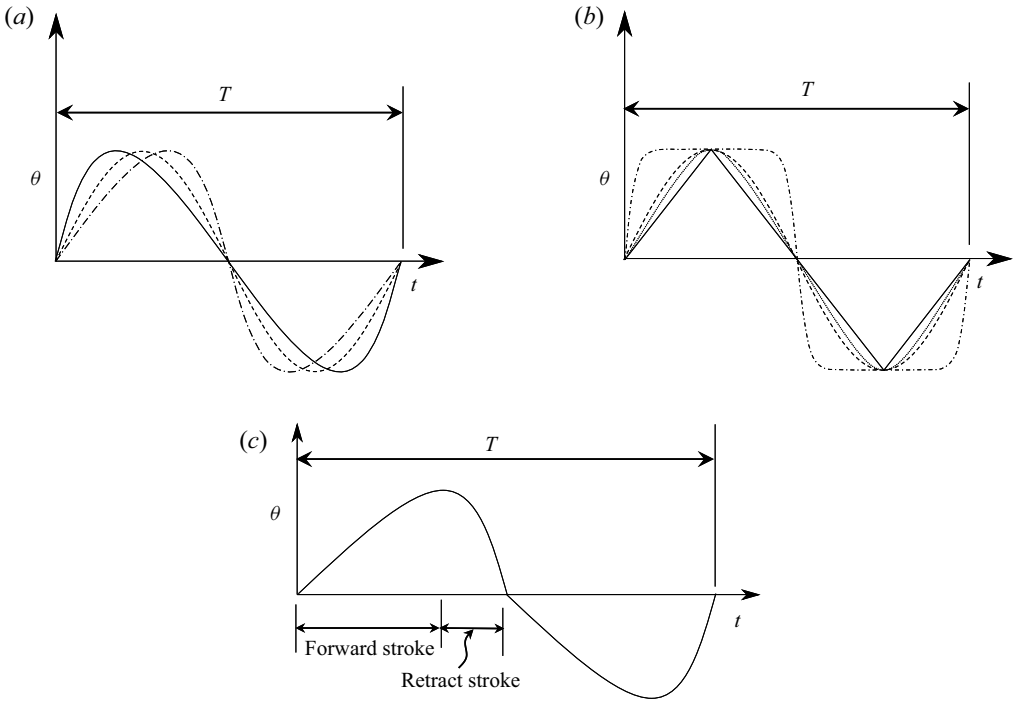

Figure 1. The pitching motions studied in the literature include (*a*) quasi-symmetric waveforms (Koochesfahani 1989; Xiao & Liao 2009) and (*b*) symmetric waveforms (Lu *et al.* 2013; Xie *et al.* 2014) from nearly square wave (dash–dotted line) to sawtooth wave (solid line). (*c*) The proposed asymmetric waveform.

a higher maximum pitch rate (maximum $\dot{\theta}(= \mathrm{d}\theta/\mathrm{d}t)$, where θ is the instantaneous pitch angle) generates stronger vortices. The boundaries of the drag–thrust transition, deflected wake transition and three-dimensional wake transition appear earlier in the St_d–A^* plane for square wave motion than for sawtooth wave motion (Chao *et al.* 2019).

The above literature on the pitching foils investigated the wake patterns, drag–thrust transition, time-average thrust and efficiency. Compared with the sinusoidal waveform, the non-sinusoidal waveforms investigated in the literature resulted in a higher thrust and a lower efficiency in most cases or a lower thrust and a higher efficiency in the other cases. It is thus challenging to enhance both thrust and efficiency at the same time. The drawback in the first category of waveforms (figure 1*a*) is that when a peak-to-peak stroke is made faster, the other stroke becomes slower, given a constant T. That is, if the faster stroke provides a better thrust, the slower stroke would worsen the thrust. The waveforms in the second category (figure 1*b*) display a peak-to-peak stroke that is the same as the other. The waveforms with higher pitch rates (e.g. nearly square waves) have higher thrust and lower efficiencies as compared to those with lower pitch rates (e.g. sawtooth wave). Note that in both categories, the motion in a peak-to-peak stroke has a second-order rotational symmetry about the point $t = T/2$. A perception of the two types of waveforms and their correspondence to the thrust and efficiency gives an idea that we should consider quarter-wise different strokes, e.g. a faster stroke from the equilibrium position to the extreme position and a slower stroke from the extreme position to the equilibrium position or *vice versa* (figure 1*c*). That is, a peak-to-peak stroke will have the first-order rotational symmetry about the point $t = T/2$, i.e. no symmetry. When animals and humans swim, their limb motion may not be sinusoidal, and the motion of their limbs

from the equilibrium to the extreme and from the extreme to the equilibrium may not be symmetric. We expect slower motion in the stroke from the equilibrium to the extreme (forward stroke) and a faster motion in the stroke from the extreme to the equilibrium (retract stroke) (figure 1*c*). This novel waveform is examined in this work. The literature have neither presented information on thrust and efficiency for the individual strokes nor focussed on the relationship between the kinematics, wake, thrust, power and efficiency. The insight into the relationship between the kinematics and thrust or efficiency is thus not well understood. Understanding of kinematics and its correspondence to thrust and efficiency may lead us to discover a way for higher thrust and efficiency simultaneously with the new waveform.

The objective of this study is to: (i) enhance both thrust and efficiency without increasing the frequency and amplitude of the pitching foil; (ii) understand the associated fluid dynamic mechanism behind the thrust enhancement and (iii) study the link between the kinematics, forces and the wake. The objective (i) 'enhancement of thrust and efficiency,' although simple, has not been attempted in the literature. Various pitching motions studied in the literature could only achieve enhancement in either thrust or efficiency. The non-sinusoidal motions studied in the literature are either symmetric about the peak (figure 1*b*) or asymmetric about the same (figure 1*a*) but both have second-order rotational symmetry. We study here a new motion (inspired by nature) that is asymmetric about both peak and equilibrium position ($t = T/2$) (figure 1*c*). The instantaneous input power and thrust generated owing to an asymmetric pitching foil are analysed and compared with those of the sinusoidal pitching foil. Furthermore, how the asymmetry of the motion influences the wake formation and size is presented in terms of vorticity evolution and wake width.

2. Methodology

2.1. *Model and parameters*

The foil is tear-shaped, with a semi-circular blunt leading edge and a tapered foil tip, extensively used in the literature (Godoy-Diana *et al.* 2008, 2009; Schnipper *et al.* 2009; Marais *et al.* 2012; Andersen *et al.* 2016; Alam & Muhammad 2020; and others). The chord (c) to thickness (d) ratio of the foil is $c/d = 5.1$, and the foil pitches about the centre (marked with a '+' sign) of the semi-circular leading edge (figure 2*a*). The peak-to-peak amplitude is defined by A. Figure 2(*b*) shows sign conventions of forces (thrust and lift), moment and power. Thrust is positive in the negative x-direction. Lift is considered positive in the y-direction while moment in the z-direction (counterclockwise rotation) is assumed positive. Power transferred from the body to the fluid is positive. The effect of gravity is ignored. The sinusoidal pitching motion can be described by amplitude and frequency. The dimensionless form of the amplitude is A^* and that of the frequency is the Strouhal number St_d, which lie in the ranges of 1.1–1.6 and 0.21–0.33, respectively. The A^* is selected based on the natural range of the tail amplitude of various fish, as reported by Floryan *et al.* (2017), while St_d is based on the natural swimmers (Godoy-Diana *et al.* 2008; Alam & Muhammad 2020). The corresponding St_A ($= St_d \times A^*$) nestles within the range observed in swimming animals, fish and cetacean (Triantafyllou, Triantafyllou & Gopalkrishnan 1991; Taylor, Nudds & Thomas 2003; Eloy 2012).

The foil is assumed to swim at constant $Re_c = 10^3$. This Re_c and the geometry used correspond to a velocity of 1.73 body lengths per second (*BL*/s), which is in the range of 0.5–3 *BL*/s for various species of fish reported by Floryan *et al.* (2017). The developed

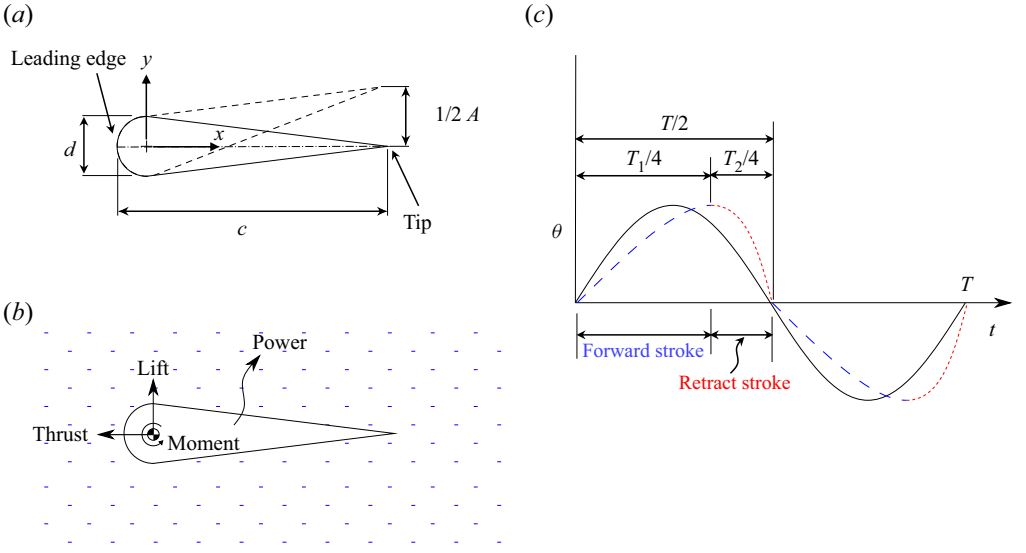

Figure 2. (*a*) Geometry and dimensions of the foil. The dashed line shows the upper extreme position of the foil during pitching motion. (*b*) Positive directions for forces, moment and power. (*c*) Sinusoidal (solid line) and modified (dashed line) waveforms.

swimming robots, employing pitching motion of the body or tail, also lie in the same range, e.g. the average speed of the *SoFi* robot fish is 0.5 *BL*/s (Katzschmann *et al.* 2018).

The inertial forces dominate the viscous forces for $Re_c \gg 1$, called the Eulerian regime (Childress 1981). The bird and fish typically operate at $Re_c \geq 10^2$ (Raspa, Godoy-Diana & Thiria 2013). The $Re_c = 10^3$ used in this study falls in the Eulerian regime. The flow around micro-air vehicles or small-unmanned underwater vehicles also lies in this regime. Moreover, Van Buren *et al.* (2018) did experiments for pitching and pitching-and-heaving wings at $Re_c \sim 10^3$–10^4, and reported that the forces on the body undergoing undulatory motion are dominated by the lateral velocity of the body, not by the free-stream flow velocity. In other words, the findings in this investigation can be applicable to a range of Re_c.

2.2. *Modified sine motion*

Figure 2(*c*) shows a sine wave (solid line) and an asymmetric wave. The asymmetric wave is a combination of two sine waves of periods T_1 and T_2 (i.e. of different frequencies), respectively, such that the foil follows the wave of period T_1 when moving from the equilibrium position to the upper or lower extreme. However, it follows the wave of period T_2 when moving from the upper or lower extreme to the equilibrium position. Naturally, the time required for the foil to reach from the equilibrium to the extreme is $T_1/4$ and that from an extreme to the equilibrium is $T_2/4$, which yields the time-period of the modified sine wave $T = (T_1 + T_2)/2$. In other words, this trajectory is an evolution of the quasi-symmetric trajectory (figure 1*a*), the first category mentioned in the introduction. Recall that in the quasi-symmetric trajectory, the time for a half-cycle (from the lower extreme to the upper extreme) was different from that for the next half-cycle (from the upper extreme to the upper extreme), with a quarter period in a half-cycle being equal to the other quarter period in the same half-cycle. Now, in the present trajectory, a quarter period (e.g. from the extreme to the equilibrium) of a half-cycle is different from the other quarter period (from the equilibrium to the upper extreme) in the same half-cycle, with the

time for a half-cycle (from the lower extreme to the upper) being essentially the same as that for the other half-cycle (from the upper extreme to the lower).

The degree of the asymmetry of the wave can be expressed by a time-period ratio ($\mathbb{T}$) as

$$\mathbb{T} = \frac{T_1}{T}. \tag{2.1}$$

The $T_1 = T_2$ gives $\mathbb{T} = 1.00$, which indicates a purely sinusoidal wave, each quarter period being the same. When $\mathbb{T} < 1.00$, the quarter stroke from the equilibrium to the extreme (referring to the 'forward stroke') is faster than the other quarter stroke from the extreme to the equilibrium (referring to the 'retract stroke'). In contrast, $\mathbb{T} > 1.00$ implies that the forward stroke is slower than the retract stroke. A discontinuity in the slope at the equilibrium position (figure 2*c*) is avoided by parametrizing the equation of foil motion in non-dimensional form as

$$\theta' = \sin 2\pi l', \tag{2.2}$$

where

$$t' = l' + \tfrac{1}{4}(\mathbb{T} - 1)\sin^2 2\pi l'. \tag{2.3}$$

In the above equations, θ' $(=\theta/\theta_{max})$ is the normalized instantaneous angular displacement of the foil, θ_{max} is the angular amplitude in radians and the parameter l' is the normalized dimensionless pseudo-time where $l' \in [0, 1]$. The dimensionless time $(t' = t/T)$ depends on $\mathbb{T}$ (2.3) that is varied from 0.80 to 1.40 in this study, which covers most of the practical limits of $\mathbb{T}$ (see Appendix A1). The use of pseudo-time to achieve a continuous function can be understood as compressing / stretching the time axis (Wald 2010). The circular frequency of pitching ω $(=2\pi/T)$ is presented in non-dimensional form as $\omega l = 2\pi l'$ ((2.2) and (2.3)). The angular velocity $(\dot{\theta})$ and acceleration $(\ddot{\theta})$ can be obtained by applying the chain rule as

$$\dot{\theta} = \frac{\partial \theta'}{\partial t'} = \frac{\dfrac{\partial \theta'}{\partial l'}}{\dfrac{\partial t'}{\partial l'}} = \frac{2\pi \cos 2\pi l'}{1 + \frac{\pi}{2}(\mathbb{T} - 1)\sin 4\pi l'}, \tag{2.4}$$

and

$$\ddot{\theta} = -\frac{4\pi^2(\pi(\mathbb{T} - 1)\cos^3 2\pi l' + \sin 2\pi l')}{\left(1 + \frac{\pi}{2}(\mathbb{T} - 1)\sin 2\pi l'\right)^2}. \tag{2.5}$$

Equations (2.2), (2.4) and (2.5) for $\mathbb{T} = 1.00$ reduce to a simple sinusoidal motion. Figure 3(*a*) shows the modified sine motion for $\mathbb{T} = 0.80 - 1.40$. Clearly, when $\mathbb{T} < 1.00$, the forward stroke is faster than the retract stroke and *vice versa*. Figure 3(*b*) shows the phase portrait of the modified sine motion, where the angular velocity is normalized as $\dot{\theta}' = \dot{\theta}/\dot{\theta}_{max}$, where $\dot{\theta}_{max}$ is the maximum angular velocity in radians per second. The phase $\phi = \tan^{-1}(\theta'/\dot{\theta}')$ is marked in degrees along with the foil rotation marked by arrows at the leading edge. It can be appreciated mathematically from (2.2), (2.4) and (2.5) and visually from figure 3 that the pitching motions (shown in figure 3) are continuously differentiable contrary to those (dashed line) shown in figure 2(*c*). The phase portrait for the sine wave ($\mathbb{T} = 1.00$) is a unit circle, whereas the modified motions ($\mathbb{T} \neq 1.00$) display distorted circles (figure 3*b*). The information on time in the phase portrait can be inferred by magnitudes of $\dot{\theta}'$ in a stroke. Compared with those for $\mathbb{T} = 1.00$, higher magnitudes of $\dot{\theta}'$ in a quarter (stroke) correspond to a shorter time in the quarter and *vice versa*. In addition, a longer arc length (in a quarter) complements a shorter time.

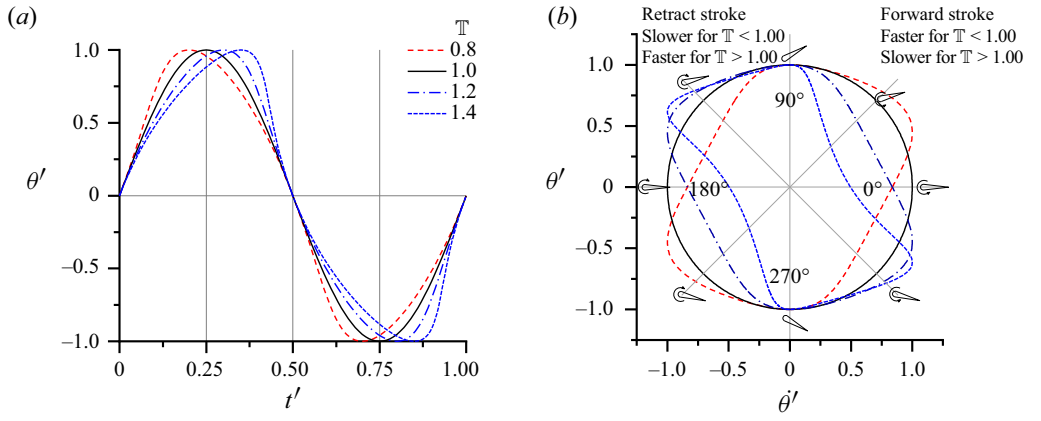

Figure 3. Modified sine motion in (*a*) waveforms and (*b*) phase portrait. Phase in degrees is marked in phase portrait, along with physical representation of the phase shown by small foil drawn along it. The arrow around the leading edge of the foil shows the instantaneous angular velocity direction.

2.3. *Numerical set-up*

Two-dimensional simulations of the unsteady, incompressible laminar flow are carried out. The non-dimensional continuity and Navier–Stokes (N-S) equations (in ANSYS Fluent) are solved using the finite-volume method (FVM), which can be written as

$$\nabla \cdot \boldsymbol{U}^* = 0 \tag{2.6}$$

and

$$\frac{\partial \boldsymbol{U}^*}{\partial t^*} + (\boldsymbol{U}^* \cdot \nabla)\boldsymbol{U}^* = -\nabla P^* + \frac{1}{Re_c}(\nabla^2 \boldsymbol{U}^*), \tag{2.7}$$

where $\boldsymbol{U}^*(x, y, t) = (u^*, v^*) = (u, v)/U_\infty$ and $P^*(x, y, t) = P/\rho U_\infty^2$ are the dimensionless velocity and pressure fields, respectively, and $t^* = tU_\infty/d$ is the non-dimensional time. The SIMPLE (Semi-Implicit Method for Pressure Linked Equations) segregated algorithm is used for pressure–velocity coupling and a second-order implicit scheme is used for the transient formulation. A structured mesh is used with the first cell height corresponding to $y^+ < 1$, see p. 540 of White (2003) for the formula and calculation of y^+. Figure 4(*a*) shows the computational domain and boundary conditions. A uniform inlet velocity (U_∞) is imposed on the upstream boundary. The side walls are modeled as frictionless walls to restrict the formation of the boundary layer. The downstream boundary is modeled as the flow outlet. While the upstream and side boundaries are $50d$ away from the pitching centre of the hydrofoil, the downstream boundary stays $150d$ away from the same centre, the blockage ratio being 1 %. The x–y coordinate system is centred at the pitching center (figure 4*a*). The motion of the foil is governed by (2.1)–(2.5) coded and hooked to the main solver. The thrust (C_T) and input power (C_P) coefficients are calculated as

$$C_T = \frac{-2 \times F_x}{\rho U_\infty^2 d}, \tag{2.8}$$

and

$$C_P = C_{Pi} + C_{Pf} = \frac{J_{zz}\ddot{\theta}\dot{\theta}}{\frac{1}{2}\rho U_\infty^3 d} + \frac{-M_z\dot{\theta}}{\frac{1}{2}\rho U_\infty^3 d} = \frac{2 \times (J_{zz}\ddot{\theta} - M_z)\dot{\theta}}{\rho U_\infty^3 d}, \tag{2.9}$$

where F_x is the drag force on the foil (in the x-direction), J_{zz} is the mass moment of inertia of the foil ($J_{zz} = 1 \times 10^{-5}$ kg-m^2, assuming the foil is made of titanium) and M_z is the

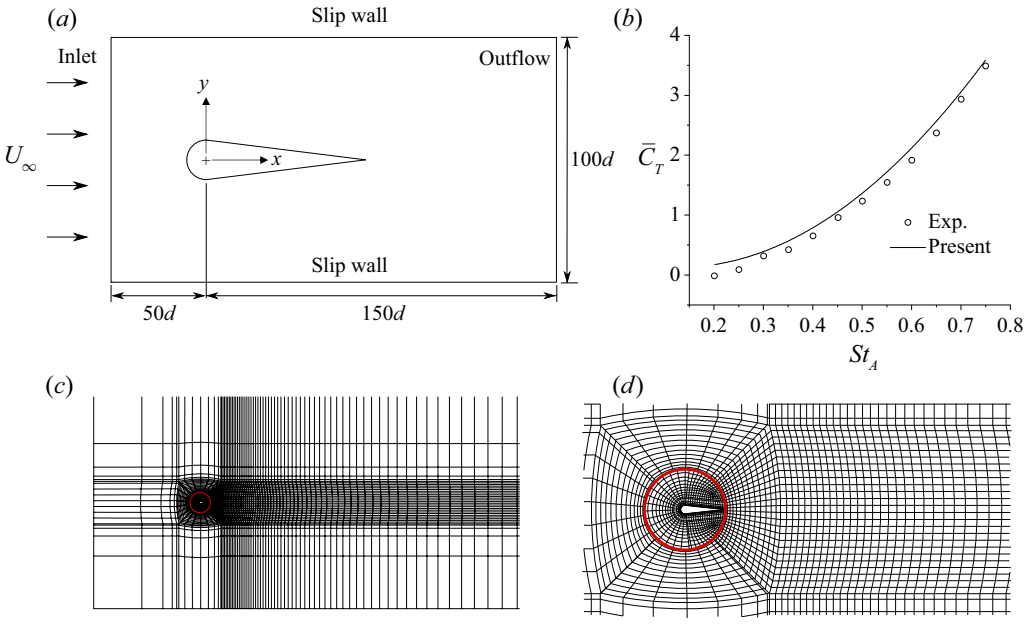

Figure 4. (*a*) Computation domain (not to scale) and boundary conditions. (*b*) Comparison between the simulated (present) and experimental (Van Buren *et al.* 2018) results. (*c*) Complete grid and (*d*) close-up view of near-field grid (every sixth line is plotted in *c* and *d*).

flow-induced moment on the foil. The instantaneous power C_P given to the fluid–structure system accelerates not only the fluid but also the foil. The power consumed by the foil inertia is $C_{Pi} = J_{zz}\ddot{\theta}\dot{\theta}/\frac{1}{2}\rho U_\infty^3 d$ and that by the fluid is $C_{Pf} = -M_z\dot{\theta}/\frac{1}{2}\rho U_\infty^3 d$. The cycle averaged quantities can be obtained by integrating the above equations over a time duration nT ($n =$ number of oscillation cycles) which can be expressed as

$$\bar{C}_T = \frac{1}{nT}\int_{t_0}^{t_0+nT} C_T(t)\,\mathrm{d}t \quad \text{and} \quad \bar{C}_P = \frac{1}{nT}\int_{t_0}^{t_0+nT} C_P(t)\,\mathrm{d}t, \tag{2.10a,b}$$

where t_0 is the initial time, chosen after the solution converges.

Naturally and mathematically,

$$\bar{C}_{Pi} = \frac{1}{nT}\int_{t_0}^{t_0+nT} C_{Pi}(t)\,\mathrm{d}t = \frac{1}{nT}\int_{t_0}^{t_0+nT} \frac{J_{zz}\ddot{\theta}\dot{\theta}}{\frac{1}{2}\rho U_\infty^3 d}\mathrm{d}t = 0. \tag{2.11}$$

Therefore, $\bar{C}_P = \bar{C}_{Pf}$, which implies that the time-averaged power input, thrust and efficiency all are independent of foil mass density or J_{zz}. The foil undergoes a forced motion, i.e. θ and its higher derivatives ($\dot{\theta}$ and $\ddot{\theta}$) are all independent of the material of foil (mass / density / J_{zz}) and the properties (ρ / υ) of the fluid (see (2.2)–(2.5)). From (2.9), we can see that $C_{Pi} \propto J_{zz}$, i.e. a higher mass moment of the inertia will result in a higher C_{Pi}. The qualitative variation of C_{Pi} is independent of the material for a perfectly elastic storage system. Equations (2.9) and (2.10*b*) both account for negative C_P (i.e. $C_P < 0$), which means that the foil receives/stores energy that can be used later. For non-elastic storage systems, we take only positive C_P into consideration, i.e. no energy is stored by the foil. Following the literature (Berman & Wang 2007; Ke *et al.* 2017; Wang, Goosen &

Keulen 2017), we define the coefficient of instantaneous positive power consumption as

$$C_P^+ = C_{Pi}^+ + C_{Pf}^+, \tag{2.12}$$

where the C_{Pi}^+ and C_{Pf}^+ are respectively the inertial and fluid components of the instantaneous positive power consumption (C_P^+). The positive power coefficient and its components are obtained by multiplying the respective coefficient / component with the signum of the C_P. The mathematical form of the positive power coefficient and its components is given as

$$C_X^+ = C_X \mathrm{sgn}(C_P), \tag{2.13}$$

where X is either P, Pi or Pf, giving C_P^+, C_{Pi}^+ and C_{Pf}^+, respectively. The time-averaged positive power coefficient can then be calculated as

$$\bar{C}_P^+ = \frac{1}{nT} \int_{t_0}^{t_0+nT} C_P^+ \, \mathrm{d}t. \tag{2.14}$$

The Froude efficiency η for elastic systems is defined as the ratio of the thrust power ($-\overline{F_x} U_\infty$) to the input power P_w, i.e. $\eta = -\overline{F_x} U_\infty / P_w$. It can be easily shown that η can be reduced as

$$\eta = \frac{\bar{C}_T}{\bar{C}_P}. \tag{2.15}$$

Note that thrust and thrust power after non-dimensionalization have the same numerical value and hence we prefer the above-mentioned form of η. Similarly, for non-elastic systems, the Froude efficiency η^+ takes the form

$$\eta^+ = \frac{\bar{C}_T}{\bar{C}_P^+}. \tag{2.16}$$

2.4. *Validation and mesh and time-step independence test*

A moving/deforming mesh system rather than a re-meshing technique is used to accommodate the motion of the foil. The former has a consistent mesh size and ability to work with quadrilateral mesh (rather than triangular mesh), unarguably superior to the latter (Murayama, Yamamoto & Kobayashi 2006; Murayama & Yamamoto 2008). However, for a moving/deforming mesh system, the time-advancement incurs additional calculations, including solving the deformations and positions for each node of the mesh for each time step. This invariably elongates the simulation time that can be reduced by increasing the time-step size. As expected, an increased time step deteriorates the solution accuracy but greatly reduces the solution convergence time. To achieve a balance between the solution accuracy and convergence time, a second-order implicit time integration scheme is used. Additionally, a relatively larger time step is used for the first 20T, which helped the solution converge faster, followed by a smaller time step to achieve time-accurate solution. Figure 4(c) shows the complete structured mesh system used. The mesh was divided into two parts, as shown in figure 4(d), separated by a non-conformal sliding interface shown by the red line. The inner part of the mesh (0.12 % of the total mesh area, inside the red circle in figure 4d) moved with the foil while the outer mesh was stationary. The first cell height normal to the foil surface was 0.004d, which is adequate for the numerical set-up used (Alam & Muhammad 2020). A similar non-conformal sliding

Validation	Mesh	Δt	$\bar{C}_T$	% difference with experiment of Van Buren *et al.* (2018)
Space	1×10^5	$T/2000$	3.62	3.43
	2×10^5	$T/2000$	3.61	3.14
	4×10^5	$T/2000$	3.62	3.43
Time	2×10^5	$T/1000$	3.65	4.29
	2×10^5	$T/2000$	3.61	3.14
	2×10^5	$T/4000$	3.59	2.57

Table 1. Grid and time independence test results ($St_d = 0.75$, $A^* = 2.44$ and $\mathbb{T} = 1.00$).

interface strategy has been employed in the literature, e.g. see Benkherouf *et al.* (2011) for heaving motion and Hanchi *et al.* (2013) for pitching motion.

Table 1 shows the mesh and time-step independence test results as well as the validation of the numerical set-up. Spatial independence was achieved by increasing the number of cells from 1×10^5 to 4×10^5. Indeed, this test was started from the independence test done for a sinusoidal oscillating foil (Alam & Muhammad 2020). The temporal independence was achieved by changing the time step Δt from $T/1000$ to $T/4000$. The results are compared with the water tunnel experiments of Van Buren *et al.* (2018), and the maximum percentage difference between the simulation and experiment is less than 5 %. The mesh with 2×10^5 cells and $\Delta t = T/2000$ is found to be adequate for the prediction of thrust with reasonable accuracy. Further increase in mesh size or time-step greatly increases the simulation time, thus outweighing the solution accuracy. We, therefore, chose the mesh with 2×10^5 cells and $\Delta t = T/2000$ for further simulations. Figure 4(*b*) shows a comparison of the present $\bar{C}_T$ with the experimental results of Van Buren *et al.* (2018). As expected, the 2-D simulation over predicts the $\bar{C}_T$, owing to the reasons including but not limited to the absence of the third dimension and the end effects caused by the finite span wing. Overall, the trend of the results matches quite well with the experimental results.

3. Results and discussion

Here, we present the results and discussion of C_T, C_P, wake and connection between C_T, C_P, wake and cycle-averaged quantities ($\bar{C}_T$, $\bar{C}_P$, η). First, a general overview is provided for the variations in C_T and C_P with $\mathbb{T}$, followed by deeper discussion of the same for some selected $\mathbb{T}$ values and their connections with the wake. Then, some interesting cases of C_P and C_T at equilibrium and extreme positions with different $\mathbb{T}$ are discussed. Finally, $\bar{C}_T$, $\bar{C}_P$ and η are discussed for the whole spectrum, including the dependence of the wake structure on $\mathbb{T}$. Finally, we discuss the wake structures, wake width, averaged wake velocity profiles and the wake deflection. The effect of inertia on non-elastic energy storage systems is discussed in § 3.4. The rest of the sections discuss the elastic energy storage systems, where the effect of inertia is non-existent.

3.1. *Instantaneous thrust, power and lift*

Figure 5(*a–j*) shows C_T (red line) and C_P (blue line) distributions in a complete oscillation cycle for $\mathbb{T} = 0.80$, 0.85, 0.90, 0.95, 1.00, 1.05, 1.11, 1.15, 1.20 and 1.40. The corresponding phase portrait $\dot{\theta}' - \theta'$ (black lines) is superimposed on the C_T and

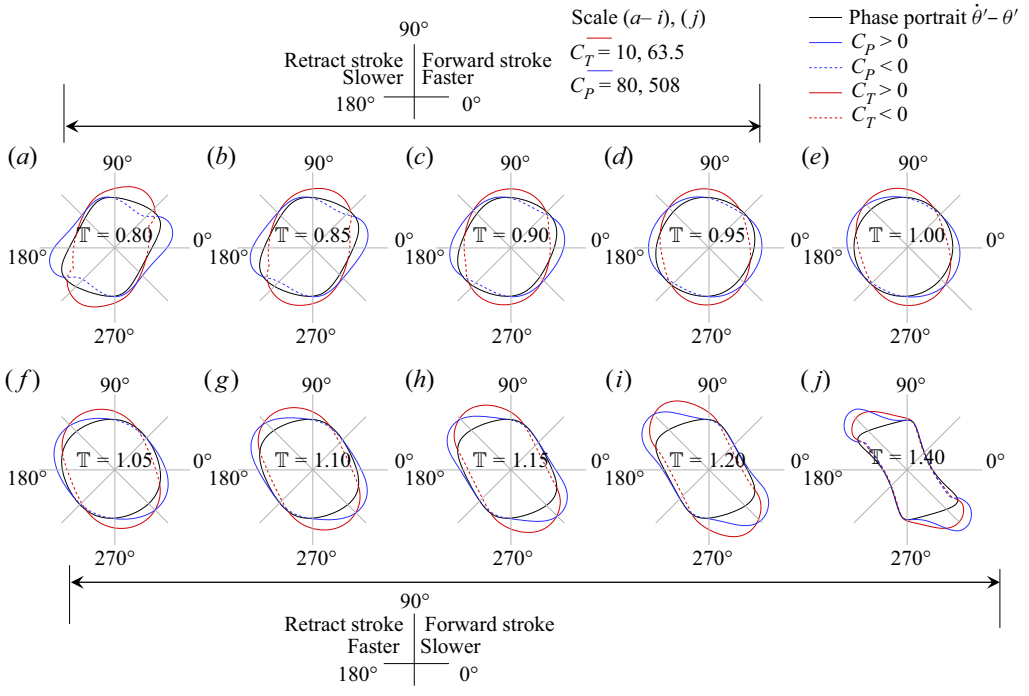

Figure 5. Instantaneous thrust (red line) and power (blue line) coefficients in the phase plane for modified sine motion with time period ratio 0.80, 0.85, …, 1.20 and 1.40 in (*a*), (*b*), …, (*j*), respectively. Positive values of both coefficients (solid lines) are outward (outside of the phase portrait) and negative values (dashed lines) are inward. Power coefficient is scaled down eight times the thrust coefficient. Here, $St_A = 0.38$.

C_P lines. The C_T lines laying outside (solid line) and inside (dashed line) of the phase portrait indicate positive and negative values of C_T, respectively. The same sign convention is applied to C_P lines. This figure also facilitates a comparison of the results between modified motion ($\mathbb{T} \neq 1.00$) and sinusoidal motion ($\mathbb{T} = 1.00$, figure 5*e*). Here, we will discuss the aerodynamics only for phase $\phi = 0°$–$180°$ (the upper half) as each profile has rotational symmetry of order two. Recall that the first and second quadrants of the phase portrait complement the faster and slower strokes, respectively, for $\mathbb{T} < 1.00$ (figure 5*a–d*) while the strokes swap their quadrants for $\mathbb{T} > 1.00$ (figure 5*f–j*).

When $\mathbb{T} < 1.00$, three distinct features can be noticed in the C_T and C_P distributions. First, the magnitudes of maximum and minimum C_T increase when $\mathbb{T}$ is decreased from 1.00 to 0.80. The same happens for C_P. For example, with $\mathbb{T}$ decreases from 1.00 to 0.80, the maximum C_T and C_P values are enhanced by 41 % and 65 %, respectively. Second, the occurrence of the maximum C_T shifts from the retract stroke at $\mathbb{T} = 1.00$ to the forward (faster) stroke when $\mathbb{T}$ is decreased from 1.00. Specifically, the maximum C_T for $\mathbb{T} = 0.80$ is at $\phi = 62°$, laying in the forward stroke (figure 5*a*), while that for $\mathbb{T} = 1.00$ is at $\phi = 107°$, early in the retract stroke (figure 5*e*). Third, the peak C_P position postpones with decreasing $\mathbb{T}$, laying at $\phi = 156°$ (late in the retract stroke) for $\mathbb{T} = 1.00$ and at $\phi = 194°$ (early in the next forward stroke) for $\mathbb{T} = 0.80$. That is, the relationship between the peak C_P position and $\mathbb{T}$ value is opposite to that between the peak C_T position and $\mathbb{T}$ value. As such, the C_T and C_P peaks occurring in the second quadrant for $\mathbb{T} = 1.00$ move away from each other when $\mathbb{T}$ is decreased to 0.80. Moreover, the positions of $C_P = 0$ and $C_T = 0$ (transition from drag to thrust) appear at $\phi = 33°$–$36°$ and $37°$–$52°$ (depending

on $\mathbb{T}$), respectively, both slightly decreasing with decreasing $\mathbb{T}$. Alam & Muhammad (2020) found that C_T and C_P are maximum at $\phi \approx 112°$ and 157° for $\mathbb{T} = 1.00$ with $St_A = 0.24$–0.53, which are consistent with the present results.

When $\mathbb{T}$ is increased from 1.00 to 1.40 (figure 5*e–j*): (i) magnitudes of maximum C_T and C_P grow by approximately 150 % and 145 %, respectively, between $\mathbb{T} = 1.00$ and 1.20, and by 990 % and 1770 %, respectively, between $\mathbb{T} = 1.00$ and 1.40; (ii) magnitudes of minimum C_T and C_P diminish between $\mathbb{T} = 1.00$ and 1.20, and enhance for $\mathbb{T} = 1.40$ as compared to $\mathbb{T} = 1.00$; (iii) the instantaneous transition from drag to thrust (i.e. $C_T = 0$) moves towards $\phi = 90°$ (extreme position); (iv) position of maximum C_T moves toward the nearest equilibrium position ($\phi = 0°$ and 180°) and (v) the gap between the C_T and C_P peaks in the retract stroke shrinks. The C_P diminishes in the forward stroke ($\phi = 0°$–$90°$) with an increase in $\mathbb{T}$, whereas grows in the retract stroke ($\phi = 90°$–$180°$). That is, faster stroke will result in a higher C_P and *vice versa*.

Overall, the above findings suggest that maximum C_T and C_P prevail in the faster stroke (i.e. forward stroke for $\mathbb{T} < 1.00$ and retract stroke for $\mathbb{T} > 1.00$). Although maximum C_T and maximum C_P both rise when $\mathbb{T}$ is increased or decreased from 1.00, the rise in the maximum C_P is higher for $\mathbb{T} > 1.00$ than for $\mathbb{T} < 1.00$, as is that in the maximum C_T. However, for $1.00 < \mathbb{T} \leq 1.20$, the degree of the increase in C_T is greater than that in C_P and hence a higher efficiency may occur for $1.00 < \mathbb{T} \leq 1.20$ than for $\mathbb{T} < 1.00$. The above observations raise a few questions. For example, which $\mathbb{T}$ is beneficial? What are their implications on swimming motion? How does the efficiency vary with $\mathbb{T}$?

3.1.1. *Correspondence between C_P and C_T*

Swimming based on C_T and C_P can be broadly categorized into four scenarios: (I) spend energy and swim upstream, i.e. $C_P > 0$ and $C_T > 0$ (normal swimming); (II) spend energy, yet drift downstream, i.e. $C_P > 0$ and $C_T < 0$ (undesirable); (III) gain energy from the fluid and drift downstream, i.e. $C_P < 0$ and $C_T < 0$ (floating); and (IV) gain energy from the fluid and swim upstream, i.e. $C_P < 0$ and $C_T > 0$ (ideal). These scenarios essentially correspond to the four quadrants of the instantaneous thrust verus power plot (C_{Pi} and C_{Pf}) as shown in figure 6(*a*), where quadrant II is undesirable and quadrant IV is ideal. The C_{Pi} (dashed red line) and C_{Pf} (green line) plots are provided only for the first half ($\phi = 0°$–$180°$) of the oscillation as the plots for the second half of the oscillation overlap with those for the first half, while this is not the case for C_L. The overlapping arises from their (C_{Pi} and C_{Pf}) generation mechanism, the product of the two waves, i.e. $C_{Pi} \propto \ddot{\theta}\dot{\theta}$ and $C_{Pf} \propto M_z\dot{\theta}$. The pressure difference between the upper and lower surfaces of the foil can readily be understood from the instantaneous lift coefficient (C_L) (figure 6*b*). A positive C_L means pressure is higher on the lower surface than on the upper surface, which produces a positive (counterclockwise) moment (see figure 2*b*). The maximum pitching angle is small, $\theta_{max} \ll 1$, and hence the trend of the pressure difference between the upper and lower surfaces can be reasonably predicted by the trend of C_L. Hereinafter, C_L will be understood as an alibi for the pressure difference, unless explicitly stated otherwise.

There are many studies on sinusoidal ($\mathbb{T} = 1.00$) pitching foil. We therefore briefly iterate some important information from the literature for a comparison purpose. For $\mathbb{T} = 1.00$, the foil at $\phi = 0°$ has negative C_T and negative C_L (figure 6*a*,*b*). The upper and lower surfaces act as pressure and suction surfaces, respectively, producing $-M_z$. As $\dot{\theta}$ is positive and maximum at $\phi = 0°$, C_{Pf} is positive but not maximum as $-M_z$ is not necessarily maximum at $\phi = 0°$ but slightly before this (figure 6*b*). At this foil position, the resultant pressure force on the side surfaces largely contributes to the lift and negligibly

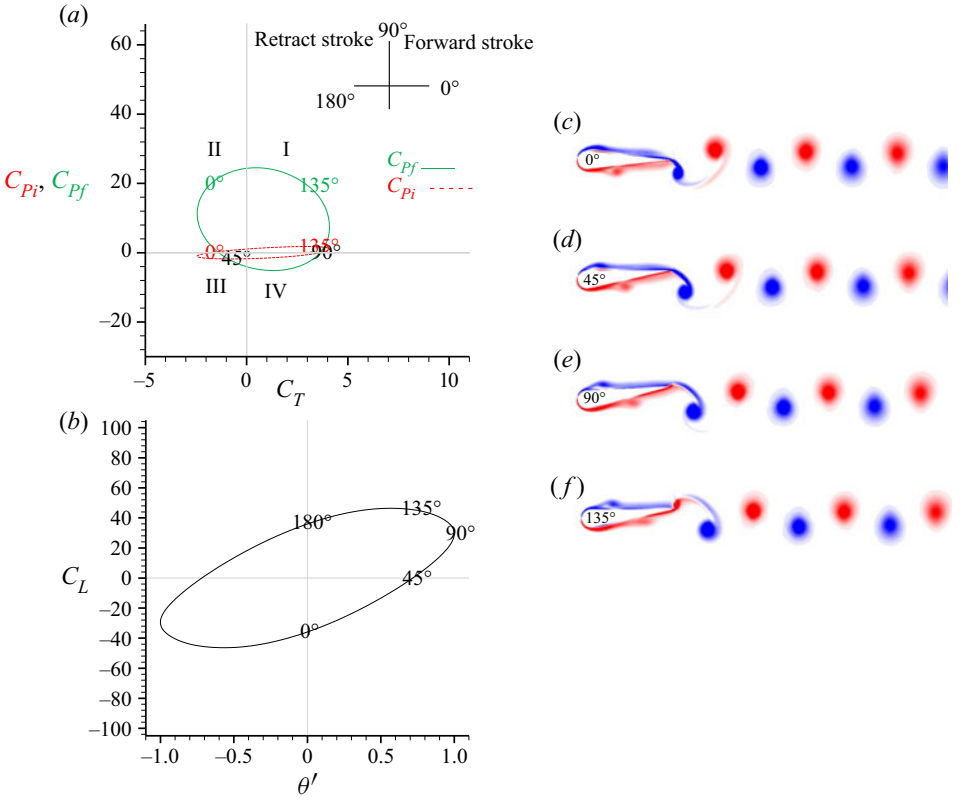

Figure 6. Sinusoidal pitching foil at $\mathbb{T} = 1.00$, variation of instantaneous (*a*) power coefficients (C_{pi}, owing to inertia and C_{Pf}, owing to fluid) with thrust coefficient and (*b*) lift coefficient with normalized angular position. (*c–f*) The wake structure for four phases namely (0°, 45°, 90° and 135°, respectively) are shown with $\Omega_z^*(= \Omega_z d/U_\infty) = [-5, 5]$, with red colour for +ve values and blue for negative. Here, $St_A = 0.38$.

to the thrust because the foil appears streamlined, having a minimum projection on the *y*-axis and a maximum projection on the *x*-axis. The pressure on the semicircular leading edge and viscous force are largely responsible for the generation of the negative thrust (Alam & Muhammad 2020). As the foil moves away from the equilibrium position, the upper shear-layer separating from the foil tip continues to roll-up (figure 6*c*). When the foil reaches $\phi = 45°$, the pressure difference across its upper and lower surfaces becomes zero (see $C_L = 0$ at $\phi = 45°$ in figure 6*b*). That is, the pressure on the upper surface decreases and/or that on the lower surface increases as ϕ increases from 0° to 45°. The C_T at $\phi = 45°$ is higher than that at $\phi = 0°$, albeit still negative. From $\phi = 0°$ to 45°, the magnitudes of both $\dot{\theta}$ and M_z decline, which leads to a decreased C_{Pf}. When the foil moves from $\phi = 45°$ to 90°, C_L increases with ϕ (figure 6*b*), which suggests that the pressure on the upper surface is progressively smaller than that on the lower surface. This pressure difference contributing to the thrust makes C_T increasingly positive (figure 6*a*). For the same reason, M_z is positive. From $\phi = 45°$ to 90°, as M_z grows and $\dot{\theta}$ declines, C_{Pf} becomes minimum between $\phi = 45°$ and 90°. That is, in the second half of the forward stroke ($\phi = 45°$–90°), the foil can move forward, gaining energy from the fluid (negative power input). In the forward stroke ($\phi = 0°$–90°), inertia being negative ($C_{Pi} < 0$) also supports the motion. From $\phi = 0°$ to 90°, the increase in C_L is accompanied by vortex growth and shedding from the upper side (figure 6*c–e*). At $\phi = 90°$–135° where the foil is in the retract stroke

(θ' decreasing), C_L keeps increasing and C_T becoming maximum at $\phi = 107°$ declines with a further increase in ϕ while C_{Pf} is positive, growing with increasing ϕ. Meanwhile, the shear layer on the lower surface starts to roll-up to form a counterclockwise vortex (red colour) behind the foil tip (figure 6*f*). From $\phi = 135°$ to 180°, both C_L and C_T drop while C_{Pf} reaches a maximum at $\phi = 158°$. The C_{Pi} is positive during retract strokes, being maximum at $\phi = 135°$.

Now we will discuss the case with $\mathbb{T} = 1.20$ (figure 5*i*), where the increase in the maximum C_T is larger than that in the maximum C_P, as compared to the case with $\mathbb{T} = 1.00$ (figure 5*e*). Figure 7 shows C_{Pf}, C_{Pi} versus C_T, and C_L versus θ'. At $\phi = 0°$–45°, C_L increases slowly, i.e. the pressure difference between the upper and lower surfaces of the foil does not change much, as do not C_{Pf} and C_T (figure 7*a*,*b*). The C_{Pi} magnitude increases negligibly, albeit negative. The C_T nevertheless rapidly enhances between $\phi = 45°$ and 90° while C_{Pf} is negative and small in magnitude. At $\phi = 90°$, both C_{Pf} and C_{Pi} become zero. It is worth pointing out that because the forward stroke for $\mathbb{T} = 1.20$ has a longer period than the retract stroke (figure 3*a*), the foil motion in the forward stroke ($\phi = 0°$–90°) is relatively slow, requiring less C_{Pi} and C_{Pf} than that for $\mathbb{T} = 1.00$ (figures 6*a* and 7*a*). Moreover, the switchover in the direction of the pressure difference is delayed as compared with that for $\mathbb{T} = 1.00$, occurring at $\phi = 45°$ and 68° for $\mathbb{T} = 1.00$ and 1.20, respectively. The foil switches to the shorter period in the retract stroke ($\phi = 90°$–180°) and experiences higher $\dot{\theta}$ and $\ddot{\theta}$ magnitudes than in the forward stroke. The C_L and C_{Pf} both thus flare up from $\phi = 90°$ to 135°, yielding a maximum C_T at $\phi = 123°$ (figure 5*i*). From $\phi = 135°$ to 180°, C_L rapidly drops; as do C_T and C_{Pf}. The C_{Pf}, however, reaches a peak at $\phi = 140°$ as the magnitude of $\dot{\theta}$ (−ve) increases and C_L (+ve) decreases between $\phi = 135°$ and 180°. At $\phi = 180°$, the C_{Pf} for $\mathbb{T} = 1.20$ is much smaller than that for $\mathbb{T} = 1.00$ (figures 7*a* and 6*a*), because of lower C_L (hence M_z) produced for $\mathbb{T} = 1.20$.

Figure 8 shows C_{Pf}, C_{Pi} versus C_T, and C_L versus θ' for $\mathbb{T} = 0.80$, which is the lowest $\mathbb{T}$ studied. At the equilibrium position ($\phi = 0°$), C_T does not change appreciably between $\mathbb{T} = 0.80$, 1.00 and 1.20 (figures 6–8), which indicates that C_T at equilibrium position is not predominantly influenced by $\mathbb{T}$ as it mainly arises from the pressure on the head of the foil and the viscous forces. The C_L magnitude at equilibrium position for $\mathbb{T} = 0.80$ is, however, quite high compared with that for the $\mathbb{T} = 1.00$ and 1.20 (see figures 6*a* and 7*a*) cases, which results in a much higher C_{Pf} for $\mathbb{T} = 0.80$ (figure 8*a*). The forward stroke for $\mathbb{T} = 0.80$ is the fast quarter, where $\dot{\theta}'$ first increases and then decreases, reaching a maximum value at $\phi = 25°$ (see phase portrait in figure 5*a* or figure 3*b*). This increase and decrease in $\dot{\theta}'$ are reciprocated by C_L variations (figure 8*b*). There is a decrease in C_T and an increase in C_{Pf} immediately after the start of the forward stroke, which is followed by a large increase in C_T and a large decrease in C_{Pf} up to the mid ($\phi = 45°$) of the forward stroke. The C_{Pf} reaches its maximum at $\phi = 15°$. The change in the C_L sign happens at $\phi = 35°$ and that for C_{Pf} takes place at $\phi = 34°$. At $\phi = 45°$–90°, the increase and decrease in C_L with ϕ are accompanied by the same in C_T. The local maxima of C_L occur at $\phi = 60°$, which is followed by C_T becoming maximum at $\phi = 62°$. In the retract (slower) stroke, C_T declines, but C_{Pf} and C_L increase. The general feature for $\mathbb{T} \neq 1.00$ is that a higher C_P (both C_{Pf} and C_{Pi}) is required to make a stroke faster. It is understood from figure 6*a* that, on average, a higher C_{Pf} is required in the retract stroke than in the forward stroke for $\mathbb{T} = 1.00$. As an additional C_P is required to make a stroke faster, C_P grows more rapidly in the retract stroke for $\mathbb{T} > 1.00$ (figure 5*f*–*j*) and in the forward stroke for $\mathbb{T} < 1.00$ (figure 5*a*–*d*).

At $\phi = 0°$, the foil is streamlined, and both viscous force and pressure force on the foil head contribute to C_T that is almost independent of $\mathbb{T}$ (figures 6*a*–8*a*). However, the C_{Pf}

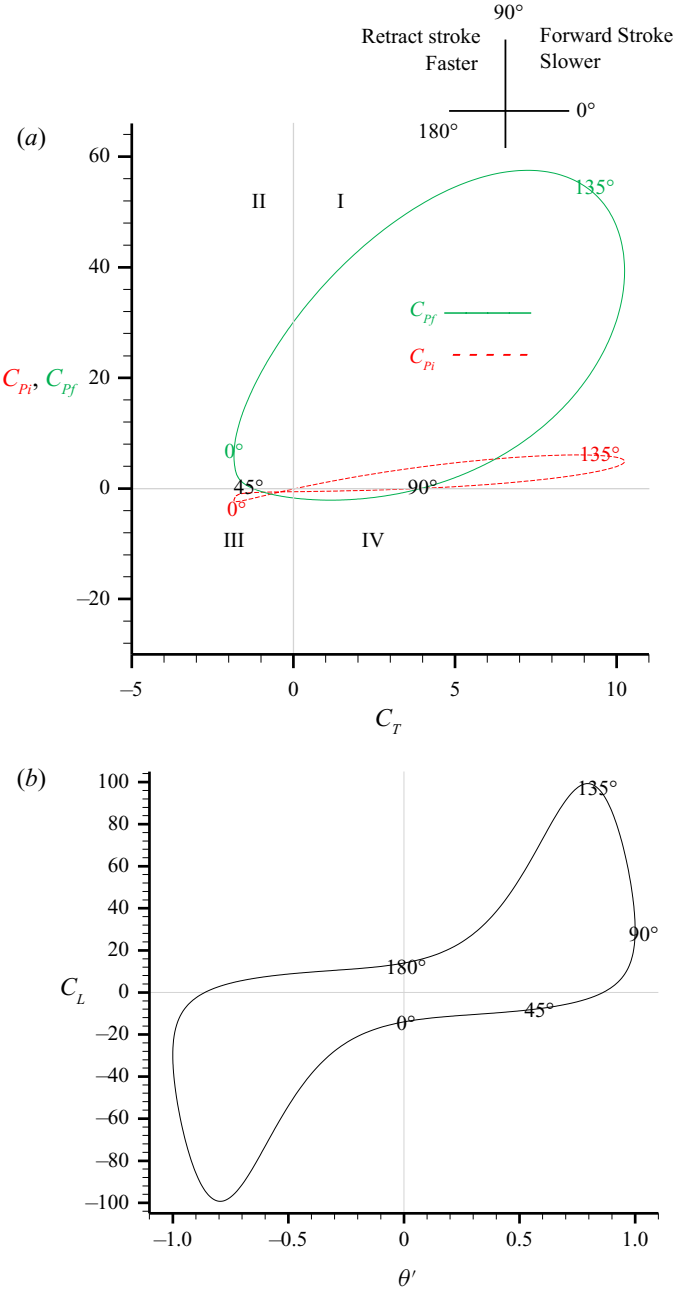

Figure 7. For $\mathbb{T} = 1.20$, variation of instantaneous (*a*) power coefficients (C_{pi}, owing to inertia and C_{Pf}, owing to fluid) with thrust coefficient and (*b*) lift coefficient with normalized angular position. Here, $St_A = 0.38$.

plays an important role in C_L generation at $\phi = 0°$. The $\dot{\theta}$ at $\phi = 0°$ is the same for all $\mathbb{T}$ (see the slopes of curves in figure 3*a*, this is not clear in figure 3*b*, owing to $\dot{\theta}_{max}$ being different for each $\mathbb{T}$) and hence the variation in C_L with $\mathbb{T}$ solely arises from the change in C_{Pf} (figures 6*b*–8*b*). At $\phi = 90°$, $\dot{\theta} = 0$ and hence $C_{Pf} = C_{Pi} = 0$, the C_L at extreme

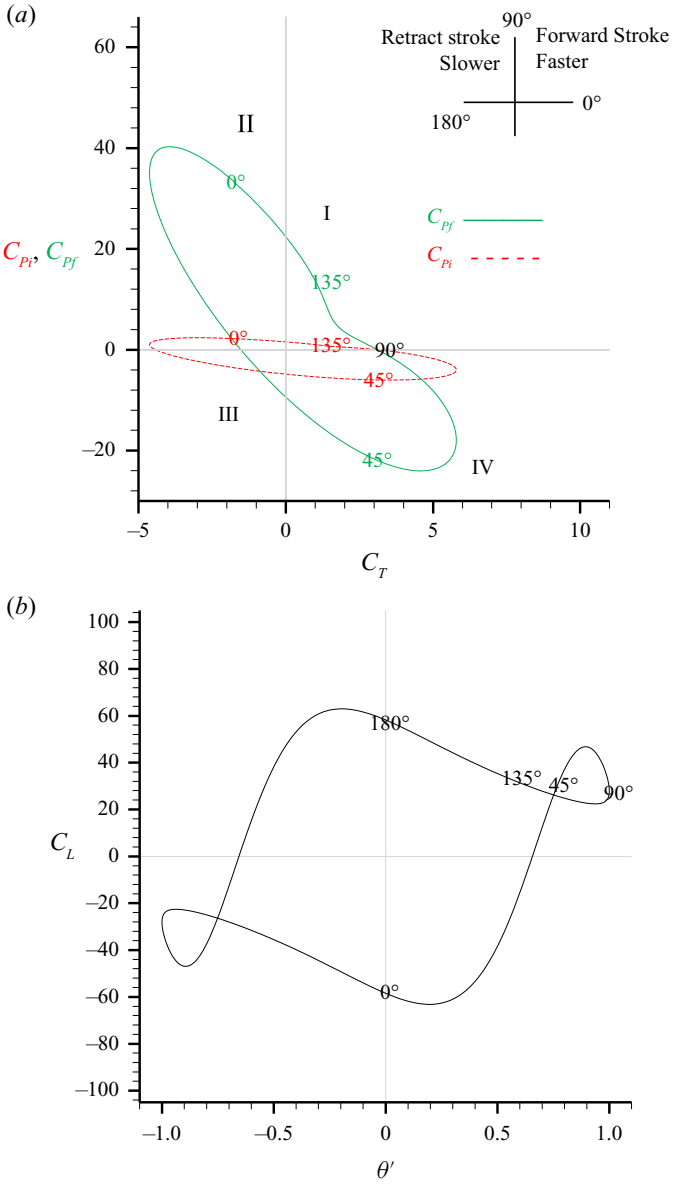

Figure 8. For $\mathbb{T} = 0.80$, variation of instantaneous (*a*) power coefficients (C_{pi}, owing to inertia and C_{Pf}, owing to fluid) with thrust coefficient and (*b*) lift coefficient with normalized angular position. Here, $St_A = 0.38$.

position is supposed to be dependent on $\mathbb{T}$, but it is not; C_L increases from 28.0 to 29.8 (0.6 %) between $\mathbb{T} = 0.80$ and 1.20, and reduces to 29.5 at $\mathbb{T} = 1.40$ (not shown).

Figure 9 shows the regimes of swimming for $\mathbb{T} = 0.80$, 1.00, 1.20 and 1.40 in one oscillation period. Each regime is presented in a shade of a particular colour to distinguish regimes. The shade of the same colour distinguishes the magnitude of C_T, with dull and bright shades representing low and high magnitudes of C_T, respectively. A comparison of figures 9(*a*) and 9(*b*) reflects that speeding up the forward stroke (i.e. $\mathbb{T} < 1.00$) does

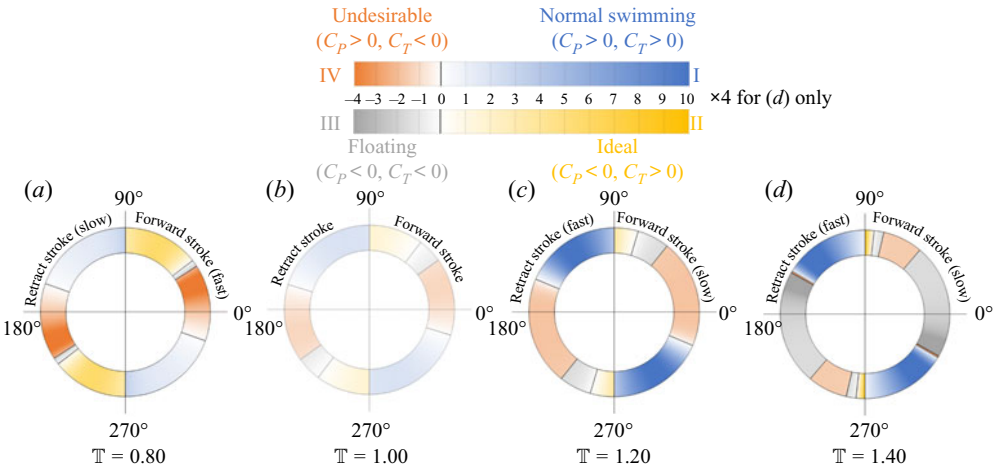

Figure 9. Regimes of swimming for (*a*) $\mathbb{T} = 0.80$, (*b*) $\mathbb{T} = 1.00$, (*c*) $\mathbb{T} = 1.20$ and (*d*) $\mathbb{T} = 1.40$ for $St_A = 0.38$. The blue, yellow, grey and orange colours represent the regimes I, II, III and IV, respectively. The shades of each colour represent the magnitude of C_T.

not appreciably affect the undesirable regime (II, orange), $\phi = -20$–$33°$ and -18–$35°$ for $\mathbb{T} = 0.80$ and 1.00, respectively, laying around the equilibrium. The magnitude of C_T is however increased ($C_T < 0$), with drag increasing. Nestling close to the middle of the forward stroke, floating regime (III, grey) shrinks from spanning 17° to 4° when $\mathbb{T}$ is decreased from 1.00 to 0.80. The ideal regime (IV, yellow) dramatically stretches from spanning 38° ($\mathbb{T} = 1.00$) to 53° ($\mathbb{T} = 0.80$), occupying the end of the forward stroke. The C_T in the ideal regime is also enhanced owing to the increased speed of the forward stroke (i.e. $\mathbb{T} < 1.00$). The normal swimming regime (I, blue) covers most of the retract stroke, approximately 70° for $\mathbb{T} = 0.80$ and 72° for $\mathbb{T} = 1.00$, while the rest of retract stroke is the undesirable regime. Regimes I (normal swimming) and IV (undesirable) do not change much between $\mathbb{T} = 0.80$ and 1.00; the magnitude of C_T however decreases in the normal swimming regime (when $\mathbb{T} < 1.00$), as compared to $\mathbb{T} = 1.00$ (figure 9*a*,*b*).

The slowing down of the forward stroke (i.e. $\mathbb{T} > 1.00$), as expected, stretches undesirable (IV) and floating (III) regimes to a span of 75° and 22°, respectively, at $\mathbb{T} = 1.20$ from a span of 53° and 17° at $\mathbb{T} = 1.00$. The magnitude of C_T (in forward stroke) also decreases for $\mathbb{T} > 1.00$ as compared to $\mathbb{T} = 1.00$ ($C_T < 0$, decreased drag). Ideal regime (II) contracts from a span of 38° at $\mathbb{T} = 1.00$ to 17° at $\mathbb{T} = 1.20$, with C_T also decreasing (figure 9*b*,*c*). In the faster retract stroke ($\mathbb{T} > 1.00$), the span of normal swimming regime (I) diminishes from 72° at $\mathbb{T} = 1.00$ to 66° at $\mathbb{T} = 1.20$, but the maximum C_T is enhanced twofold. As such, undesirable regime (IV) expands from $\mathbb{T} = 1.00$ to 1.20, laying mostly in the forward stroke (figure 9*b*,*c*).

The pattern modifies significantly when the forward stroke is further slowed down to the case of $\mathbb{T} = 1.40$, where the floating regime (III) nestling around the equilibrium position now spans most of the forward stroke i.e. from $-30°$ to 50° (figure 9*d*). The undesirable regime (IV) shrinks and shifts further towards the end of the forward stroke, spanning 50°–77°. One more floating regime (III) and ideal regime (II) are observed at the end of the forward stroke, both being very narrow. The normal swimming regime (I) further shrinks from 66° for $\mathbb{T} = 1.20$ to 59° for $\mathbb{T} = 1.40$, followed by an infinitesimal undesirable (IV) regime spanning only 2°. The floating regime (III) covers the rest of the retract stroke and expands much further into the next forward stroke. The magnitude of C_T is much larger for

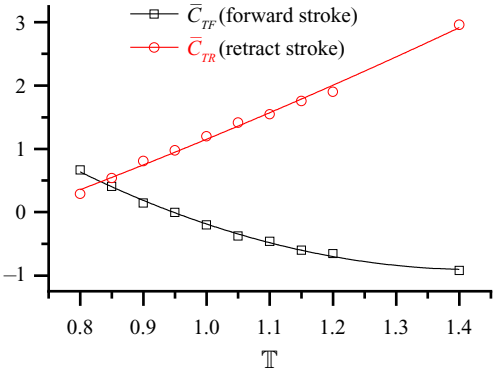

Figure 10. Strokewise averaged thrust dependence on $\mathbb{T}$ for $St_A = 0.38$.

$\mathbb{T} = 1.40$ than for $0.80 \leq \mathbb{T} \leq 1.20$. Hence, figure 9(*d*) uses a scale four times the scale for figure 9(*a–c*).

The following points can be distilled from the above discussion. The undesirable and ideal modes are fashionably opposite to each other; the former provides power but obtains no net thrust while the latter receives both power and thrust. The forward stroke ($\phi = 0°$ to 90°) for $\mathbb{T} = 1.00$ generally envelops undesirable and ideal regimes separated by a narrow floating regime, while the retract stroke largely provides normal swimming (figure 9*b*). When $\mathbb{T}$ is increased from 0.80 to 1.20, the spans of the undesirable and floating regime (both involving $C_T < 0$) in the forward stroke dramatically grow and that of the ideal regime (involving $C_T > 0$) contracts. That is, the corresponding change in the forward stroke essentially degrades thrust. However, with $\mathbb{T}$ increasing from 0.80 to 1.20, the spans of regimes I ($C_T > 0$) and II ($C_T < 0$) in the retract stroke do not change much (figure 9), but the magnitude of thrust is radically enhanced in regime I (see figure 5 or figure 9), which is the main reason for enhancement of the time-averaged thrust at $\mathbb{T} = 1.20$. The two scenarios (decreasing and increasing thrust in the forward and retract strokes with increasing $\mathbb{T}$) further point to the occurrence of the minimum $\bar{C}_T$ between $\mathbb{T} = 0.80$ and 1.20. For $\mathbb{T} = 1.40$, $C_T < 0$ in regimes III and IV of the forward stroke further degrades when compared with that for $\mathbb{T} = 1.20$. The retract stroke for $\mathbb{T} = 1.40$, unlike the same for $\mathbb{T} = 1.20$, has a floating regime ($C_T < 0$). The C_T in the normal swimming regime is very large, which makes the $\bar{C}_T$ large for $\mathbb{T} = 1.40$.

Figure 10 shows the individual contributions $\bar{C}_{TF}$ and $\bar{C}_{TR}$ of the forward and retract strokes, respectively, to $\bar{C}_T$ for $St_A = 0.38$, where $\bar{C}_{TF}$ and $\bar{C}_{TR}$ are the thrust force coefficients integrated over the forward and retract strokes of a complete oscillation cycle, respectively, i.e.

$$\bar{C}_{TF} = \frac{2}{\pi}\left[\int_0^{\pi/2} C_T \,\mathrm{d}\phi + \int_{\pi}^{3\pi/2} C_T \,\mathrm{d}\phi\right] \quad \text{and} \quad \bar{C}_{TR} = \frac{2}{\pi}\left[\int_{\pi/2}^{\pi} C_T \,\mathrm{d}\phi + \int_{3\pi/2}^{2\pi} C_T \,\mathrm{d}\phi\right]. \tag{3.1a,b}$$

As discussed above, the $\bar{C}_{TF}$ and $\bar{C}_{TR}$ contributions to $\bar{C}_T$ decrease and increase, respectively, when $\mathbb{T}$ is increased. The magnitude of increase with $\mathbb{T}$ is however greater than that of the decrease, which explains why $\bar{C}_T$ grows with $\mathbb{T}$. The figure also indicates that $\bar{C}_T$ would be a minimum at $\mathbb{T} = 0.83$.

There are four general locomotion behaviours for swimming fish observed in nature: steady swimming, kick and glide (intermittent swimming), fast start (including C-start and

S-start) and braking (e.g. Jayne, Lozada & Lauder 1996; Shadwick & Lauder 2006). The overview of figure 9 echoes some interesting observations in natural biological swimming. First, for a fast start that is typically associated with the escape response of a fish, high power is required to hastily bend the fish body to its limit, and the thrust should be generated in-phase with the body movement (power). This is the case for $\mathbb{T} > 1.00$ (figure 9*c*,*d*), where C_T and C_P are almost in-phase and thrust is generated near the extreme position of the foil (figure 5*f*–*j*). In addition, the fast-start response depending on the fish body curvature and the escape route is characterized as C-start (fish escapes from its wake) or S-start (fish escapes side-ways). This is achieved by high lateral forces or moments achieved when the foil tail is near its extreme position ($\mathbb{T} > 1.00$, see figure 7*b* showing high C_L near the extreme position). Second, for steady swimming, the steady motion of the foil tail guarantees the impulse of thrust that sustains steady swimming, just as in the case of $\mathbb{T} = 1.00$ (figure 9*b*). Third, for braking, the drag should be achieved near the equilibrium position which is the case for $\mathbb{T} = 0.80$, where $C_T < 0$, i.e. undesirable regime concentrated near the equilibrium position (figure 9*a*). Also, the fact that for $\mathbb{T} = 0.80$, the maximum drag is generated when the most power is applied (i.e. C_T and C_P are out of phase, see figure 5*a*) further shows the similarity of $\mathbb{T} < 1.00$ motion to the braking phenomenon.

3.2. *Effects of θ', $\dot{\theta}'$ and $\ddot{\theta}'$ on instantaneous thrust, power and lift*

Figure 11 shows the contour plots of instantaneous thrust, power and lift on the $\mathbb{T} - t'$ plane for $St_A = 0.38$, overlaid with solid, dashed and dash-dotted lines representing extremes of θ', $\dot{\theta}'$ and $\ddot{\theta}'$ ($= \ddot{\theta}/\ddot{\theta}_{max}$, where $\ddot{\theta}_{max}$ is the maximum angular acceleration, rads^{-2}), respectively, with maximum and minimum values represented by green and black lines, respectively. Here, the subscripts 'max' and 'min' denote maximum and minimum, respectively. The dotted line marks the half time-period (end of the retract stroke), while the extremes of θ' mark the ends of the forward strokes. The contours are coloured such that shades of red and blue represent positive and negative values of the contour variable. When $\mathbb{T} < 1.00$, the extremes (positive and negative) of $\dot{\theta}'$ and $\ddot{\theta}'$ shift from the stroke boundaries ($\theta' = 0$ and $\theta' = \theta'_{max}$) to the fast forward stroke (figure 11). In contrast, when $\mathbb{T} > 1.00$, the extremes of $\dot{\theta}'$ and $\ddot{\theta}'$ fall in the fast retract stroke.

The C_T for $\mathbb{T} = 1.00$ is minimum in the forward stroke at $t' \approx 0.062$ ($\phi \approx \pi/8$) and maximum in the retract stroke $t' \approx 0.31$ ($\phi \approx 5\pi/8$) (figure 5*e*), see also Alam & Muhammad (2020). With $\mathbb{T}$ decreasing from 1.00, C_T remains minimum at $t' \approx 0.062$ while the maximum C_T gradually shifts from the retract stroke to the preceding forward stroke, as does $\ddot{\theta}'_{min}$. The reason for the occurrence of the maximum C_T following $\ddot{\theta}'_{min}$ is the fluid inertia lagging the foil inertia, which generates a large pressure difference between the two surfaces of the foil (Alam & Muhammad 2020). The relationship between fluid inertia, foil motion and fluid forces is detailed by Alam & Muhammad (2020). When $\mathbb{T}$ is increased from 1.00, both $\ddot{\theta}'_{min}$ and $\dot{\theta}'_{min}$ come into being in the retract stroke, and the maximum C_T lagging $\ddot{\theta}'_{min}$ approaches $\dot{\theta}'_{min}$ at $\mathbb{T} = 1.40$ (figure 11*a*). Particularly for $1.30 \leq \mathbb{T} \leq 1.40$, the $\dot{\theta}'$ in the retract stroke is much higher (see the slope for $\mathbb{T} = 1.40$ in figure 3*a*), which makes it difficult for the fluid inertia to keep up with the foil, resulting in a more time delay (t') between $\ddot{\theta}'_{min}$ and maximum C_T, compared with that for $1.00 < \mathbb{T} < 1.30$.

The C_{Pf} at the start of the forward stroke is positive and negative for $0.80 \leq \mathbb{T} \leq 1.30$ and $1.30 < \mathbb{T} \leq 1.40$, respectively (see also $\phi = 0°$ in figures 5*j* and 8*a*), linked to the motion state at the end of the earlier retract stroke, which will be discussed later.

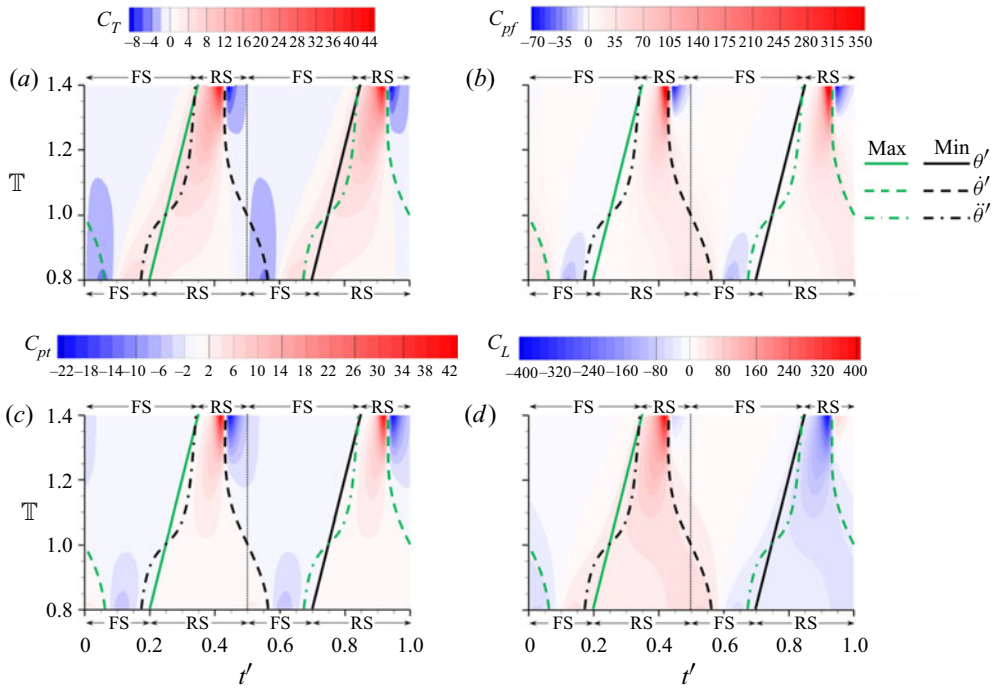

Figure 11. Effect of instantaneous θ', $\dot{\theta}'$, and, $\ddot{\theta}'$ on (*a*) C_T, (*b*) C_{Pf}, (*c*) C_{Pi} and (*d*) C_L for $St_A = 0.38$. The straight, dashed and dash–dotted lines represent extremes of θ', $\dot{\theta}'$ and $\ddot{\theta}'$, with green and black colours of lines for maximum and minimum values. FS and RS stands for Forward and Retract Stroke, respectively.

The C_{Pf} for $\mathbb{T} > 1.30$ is positive in the middle of the slow forward stroke, which results from the slow-motion foil pushing the fluid. The C_{Pf} switches to negative before the end of the forward stroke (i.e. at $t' \approx t'(\theta'_{max}) - 0.125$) because of the decelerating foil resisting the fluid inertia. The C_{Pf} becomes zero at the boundary between the forward and retract strokes (see $\dot{\theta}'_{max}$ line in figure 11*b*) as $\dot{\theta}' = 0$ (see (2.9)). The region of the retract stroke largely consists of positive C_{Pf}, except for $1.30 < \mathbb{T} \leq 1.40$ in which the C_{Pf} is negative beyond $\dot{\theta}'_{max}$ (figure 11*b*). The change in the behaviour of C_{Pf} with t' in the retract stroke for $\mathbb{T} > 1.30$ is attributed to the change in the foil acceleration from negative to positive at $\dot{\theta}'_{min}$ at which the fluid (negatively accelerated before $\dot{\theta}'_{min}$) bumps into the foil that moves at a slower pace than the fluid.

Being the product of $\dot{\theta}'$ and $\ddot{\theta}'$ (2.9), C_{Pi} is zero when one of them is zero, i.e. at $\dot{\theta}' = 0$ (θ'_{max} and θ'_{min} lines) and at $\ddot{\theta}' = 0$ ($\dot{\theta}'_{max}$ and $\dot{\theta}'_{min}$ lines). The C_{Pi} for $\mathbb{T} > 1.00$ is negative in the forward stroke because of the foil deceleration. However, for $\mathbb{T} < 1.00$, the C_{Pi} is initially positive before $\dot{\theta}'_{max}$ and becomes negative after $\dot{\theta}'_{max}$where $\dot{\theta}'$ diminishes. The retract stroke is engulfed with positive C_{Pi} as $\dot{\theta}'$ increases in magnitude until $\dot{\theta}'_{min}$ (figure 11*c*). For $\mathbb{T} = 1.00$, the C_{Pi} is negative and positive in the forward and retract strokes, respectively, dictated by negative and positive $\ddot{\theta}'$ at the corresponding strokes. In constrast, for $\mathbb{T} \neq 1.00$, the sign of C_{Pi} is contingent on $\dot{\theta}'$ and $\ddot{\theta}'$ in the individual strokes, as explained above.

Because $\theta_{max} \ll 1$, the C_L is directly linked to the difference in pressure between the upper and lower surfaces of the foil. Because the foil undergoes forced motion, the C_L will typically acts opposite to the motion with some phase lag because of the fluid inertia (Alam

& Muhammad 2020). The C_L is essentially positive (see figure 2*b* for sign convention) for most of the downward stroke including retract and forward strokes between θ'_{max} and θ'_{min}, with C_L lagging θ' (see figure 11*d*). The C_L largely follows the trend of C_{Pf} variation with t' in the retract stroke for $\mathbb{T} > 1.30$, with C_L becoming momentarily negative after $\dot{\theta}'_{min}$. As expected, the amplitude of C_L increases as the magnitude of $\dot{\theta}'$ enhances, i.e. with the retract stroke getting shorter. The $\dot{\theta}'$, $\dot{\theta}'$ and $\ddot{\theta}'$ all affect C_T, C_{Pf}, C_{Pi} and C_L. The C_{Pi} is influenced by $\dot{\theta}'$ and $\ddot{\theta}'$ only, following (2.9), whereas C_T, C_L and C_{Pf} all have a strong dependence on $\mathbb{T}$.

3.3. *Effect of* $\mathbb{T}$ *on time-averaged thrust, power coefficient and efficiency*

Very complex scenarios have been observed in the instantaneous C_T and C_P when $\mathbb{T}$ is increased or decreased from 1.00. It would be interesting to see the dependence of time-averaged hydrodynamic parameters on $\mathbb{T}$. Figure 12 shows dependence of $\bar{C}_T$, $\bar{C}_P$ and η on $\mathbb{T}$ for the three selected cases with $St_A = 0.23$, 0.36 and 0.43 lying within the St_A range of flying and swimming animals reported in the literature (see e.g. Triantafyllou, Triantafyllou & Grosenbaugh 1993; Taylor *et al.* 2003). At a given $\mathbb{T}$, $\bar{C}_T$ escalates with increasing St_A. With $\mathbb{T}$ increasing from 0.80 to 1.40, $\bar{C}_T$ first declines and then grows, being minimum at $\mathbb{T} = 0.85$ for all St_A values (figure 12*a*). This however is not in conflict with the earlier finding (from figure 10), because the simulated $\mathbb{T}$ value closest to 0.83 is 0.85 and hence we see minimum $\bar{C}_T$ occurring at $\mathbb{T} = 0.85$. The border of the minimum $\bar{C}_T$ coincides with that separating 2P and 2S wakes, which will be discussed in the later sections. For sinusoidal motion, C_T is large and small when the foil is close to the extreme and equilibrium, respectively ($\mathbb{T} = 1.00$, figure 6*a*). As the $\mathbb{T}$ is increased (say from 0.83 to 1.40), the increased contribution of the retract stroke to $\bar{C}_T$ is slightly higher than the decreased contribution of the forward stroke to $\bar{C}_T$ (figure 10). Hence the rate of increase in $\bar{C}_T$ with $\mathbb{T}$ grows with increasing $\mathbb{T}$ (figure 12*a*). The wider 2P wake forming for $\mathbb{T} \leq 0.85$ (shown later) results in $\bar{C}_T$ growing for $\mathbb{T} \leq 0.85$ (figure 12*a*). This can also be explained in terms of the shift of the C_T peak toward the extreme position (figure 5*a*). When appearing near the extreme, the peak becomes broad because of the small velocity magnitude of the foil. When $\mathbb{T}$ is increased from 0.85 to 0.95, the C_T peak declines in height but shifts toward the extreme ($\phi = 90°$) (figure 5). The effects of two scenarios cancel each other; the ensuing effect on $\bar{C}_T$ is thus very small between $\mathbb{T} = 0.85$ and 0.95 (figure 12*a*). However, for $\mathbb{T} = 0.95 - 1.40$, although the C_T peak moves away from the extreme, its height grows rapidly, such that the value of C_T at $\phi = 90°$ does not change appreciably (figure 5). The $\bar{C}_T$ increase with the increase in $\mathbb{T}$ is thus rapid for $\mathbb{T} > 0.95$ (figure 12*a*).

The $\bar{C}_P$ follows the same trend except that it becomes a minimum at $\mathbb{T} = 1.00$. Recalling figure 5, one can see that when $\mathbb{T}$ is increased from 0.80 to 0.95, the C_P peak occurring in the first quadrant moves away from the extreme, with the peak height diminishing. Both cause $\bar{C}_P$ to decline with $\mathbb{T}$ (figure 12*b*). The scenario is opposite for $\mathbb{T} > 1.00$, the peak budging toward the extreme with the peak height growing (figure 5). The $\bar{C}_P$ therefore grows, with a minimum $\bar{C}_P$ prevailing at $\mathbb{T} = 1.00$ (figure 12). The η for $St_A = 0.36$ increases monotonically with $\mathbb{T}$ while that for $St_A = 0.43$ does the same for $0.80 \leq \mathbb{T} \leq 1.20$ but declines for $\mathbb{T} > 1.2$ (figure 12*c*). The η decreases to a minimum at $\mathbb{T} = 0.90$ for the drag cases (e.g. $St_A = 0.23$ in figure 12*c*) then increases rapidly with increasing $\mathbb{T}$. Interestingly, the drag–thrust boundary can be crossed at a smaller St_A by changing the foil kinematics $\mathbb{T}$ (figure 12*a*). Because we are not interested in drag-creating conditions, no further examination will be made for this.

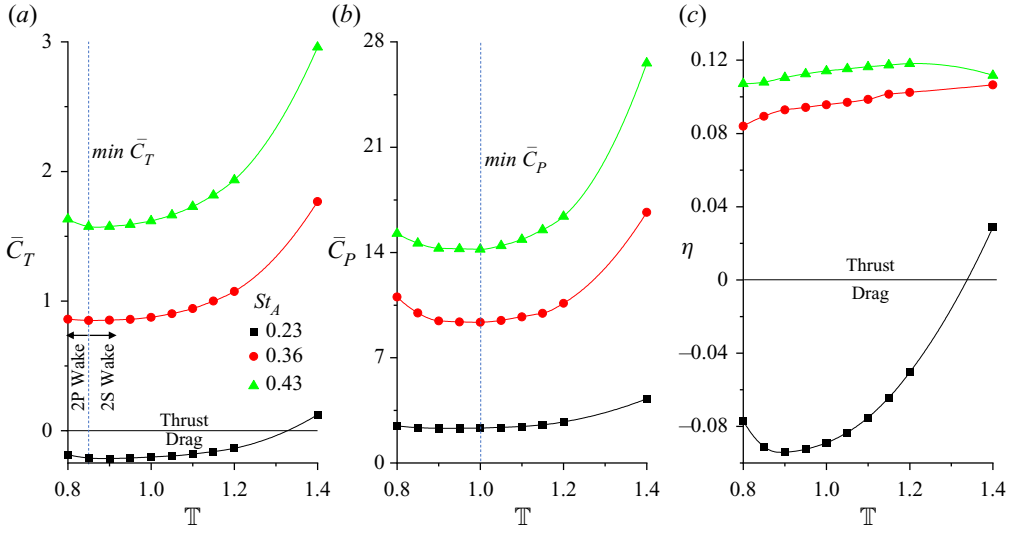

Figure 12. Dependence on $\mathbb{T}$ of (*a*) thrust coefficient, (*b*) input power coefficient and (c) efficiency. To avoid the clutter, only three different St_A values are plotted.

Figures 13(*a*)–13(*c*) presents the full spectrum of $\bar{C}_T$, $\bar{C}_P$ and η on the $\mathbb{T} - St_A$ plane. The solid line represents the drag-thrust boundary. The dependence of $\bar{C}_T$, $\bar{C}_P$ and η on St_A at $\mathbb{T} = 1.00$ is well known and also can be seen here, all increasing with St_A. The increase is, however, sensitive to $\mathbb{T}$. A greater increase in $\bar{C}_T$ and $\bar{C}_P$ with St_A is observed when $\mathbb{T}$ is increased from 1.00, shifting the drag–thrust boundary to a smaller St_A. The same happens when $\mathbb{T}$ is decreased from 1.00 but the increase in $\bar{C}_T$ is smaller than that for $\mathbb{T} = 1.00$. As such, a significant enhancement in η is observed with increasing $\mathbb{T}$ from 1.00 while the opposite is the case when $\mathbb{T}$ is decreased from 1.00. For $St_A > 0.40$, an increase in $\mathbb{T} > 1.20$ leads to η declining. The benefit of the modified motion starts to decrease as the St_A is increased above $\sim$0.45. The maximum efficiency is achieved at $St_A = 0.63$ for sinusoidal motion $\mathbb{T} = 1.00$. The minimum $\bar{C}_T$ occurs at $\mathbb{T} = 0.85$, coinciding with the 2P–2S wake boundary (figure 13*a*). The minimum $\bar{C}_P$ occurs at $\mathbb{T} = 1.00$ for all St_A (figure 13*b*). When $\mathbb{T}$ is decreased below 1.00, the magnitude of maximum and minimum value of C_P increase (figure 5*a–d*). In contrast, for $\mathbb{T} > 1.00$, the increase in $\mathbb{T}$ leads to an increase and decrease in the maximum and minimum magnitudes of C_P values, respectively (figure 5*f–j*); however, the increase in C_P maximum values is larger than the decrease in the C_P minimum values. This also leads to an increase in the overall $\bar{C}_P$ with an increase in $\mathbb{T}$, but at a rate slightly higher than when $\mathbb{T}$ in decreased below 1.00 (figure 12*b*). The η increases with $\mathbb{T}$ and St_A for $0.3 \leq St_A < 0.4$ (Figure 13*c*). When St_A is further increased, the maximum η slowly shifts from $\mathbb{T} = 1.40$, $St_A = 0.4$ to $\mathbb{T} = 1.00$, $St_A = 0.53$. The decrease in η for $\mathbb{T} > 1.00$ at high St_A arises from the large $\dot{\theta}$ in the retract stroke (figure 3), with $\bar{C}_P$ increasing more rapidly than $\bar{C}_T$.

3.4. *Effect of foil inertia on power and efficiency*

The non-elastic systems are affected by the foil inertia since $C_P < 0$ cannot be used. The foil inertia thus plays an important role in defining the efficiency. It should be noted that we use inertia and moment of inertia interchangeably in this section. We investigate only a

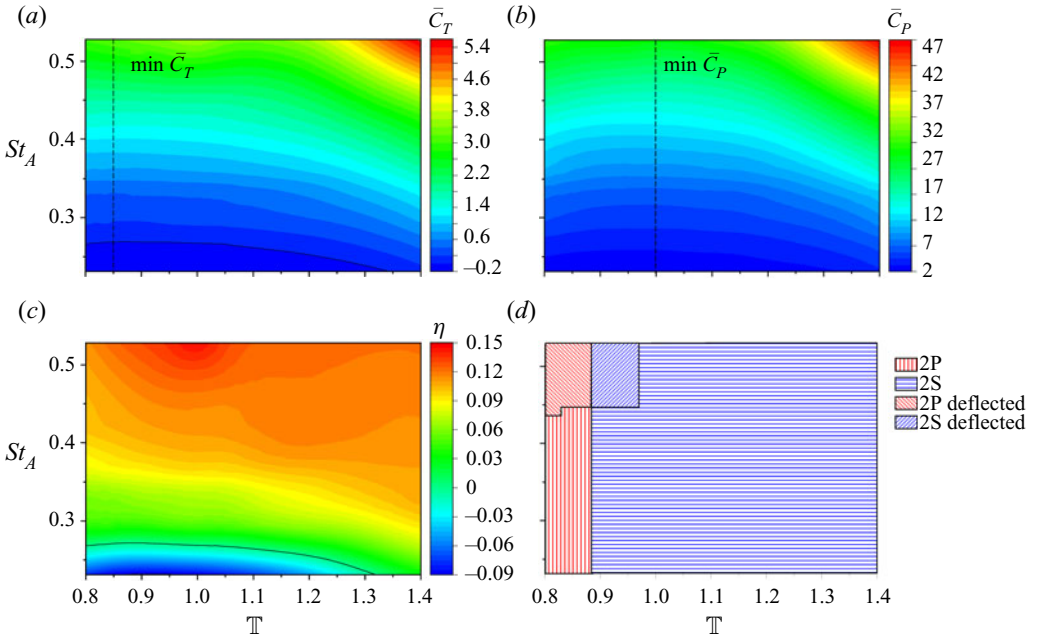

Figure 13. Contours of average (*a*) thrust coefficient, (*b*) input power coefficient and (*c*) efficiency. The black solid line is the drag–thrust boundary. The dashed lines represents the minimum values of power or thrust against St_A. (*d*) Detailed wake map on the $St_A - \mathbb{T}$ plane.

single geometry with a uniform density, thus the increase in mass (i.e. density) is reflected in the moment of inertia of the foil. We consider three different moments of inertia, denoted by materials I, II and III. The foil of material I has a very small moment of inertia ($J^I_{zz} = 1 \times 10^{-5}$ kg - m^2), and the resulting inertial component of the power is negligible as compared to the fluid component of the power i.e. $\bar{C}^+_{Pi} \ll \bar{C}^+_{Pf}$. The foil of material II has a large moment of inertia ($J^{II}_{zz} = 10J^I_{zz}$), making the inertial and fluid components of the power to be almost equal to each other i.e. $\bar{C}^+_{Pi} \approx \bar{C}^+_{Pf}$. The foil of material III has a very large moment of inertia ($J^{III}_{zz} = 10J^{II}_{zz}$), such that the fluid component of the power becomes negligible as compared to the inertial component of the power i.e. $\bar{C}^+_{Pi} \gg \bar{C}^+_{Pf}$. Figure 14 shows C^+_P (black line), C^+_{Pf} (blue line) and C^+_{Pi} (red line) over a complete pitching cycle in the case of $St_A = 0.38$ for materials I (first column), II (second column) and III (third column), and for $\mathbb{T} = 0.80$ (first row), 1.00 (second row) and 1.20 (third row). The C^+_{Pi} and C^+_{Pf} both are zero at $\phi = 90°$ and 270° (for all materials and $\mathbb{T}$), i.e. at extreme positions of the foil due to $\dot{\theta}' = 0$. When foil moves away from the extreme positions, C^+_{Pi} and C^+_{Pf} both increase from zero (see e.g. $t' = 0.20$, 0.25 and 0.30 for $\mathbb{T} = 0.80$, 1.00 and 1.20, respectively, in figure 14 for all materials), having positive value owing to $\dot{\theta}$, $\ddot{\theta}$ and $-M_z$ having the same direction (see (2.9) and (2.13)). For all materials, the first peak of C^+_{Pi} occurs at $t' = 0.02$, 0.375 and 0.39 for $\mathbb{T} = 0.80$, 1.00 and 1.20, respectively, while that of C^+_{Pf} occurs at $t' = 0.035$, 0.44 and 0.40 for $\mathbb{T} = 0.80$, 1.00 and 1.20, respectively. That is, C^+_{Pi} leads C^+_{Pf} (Alam & Muhammad 2020). The first peak of C^+_P for materials I, II and III respectively occurs at $t' \approx 0.035$, 0.025 and 0.02 for $\mathbb{T} = 0.80$, at $t' \approx 0.435$, 0.405 and 0.38

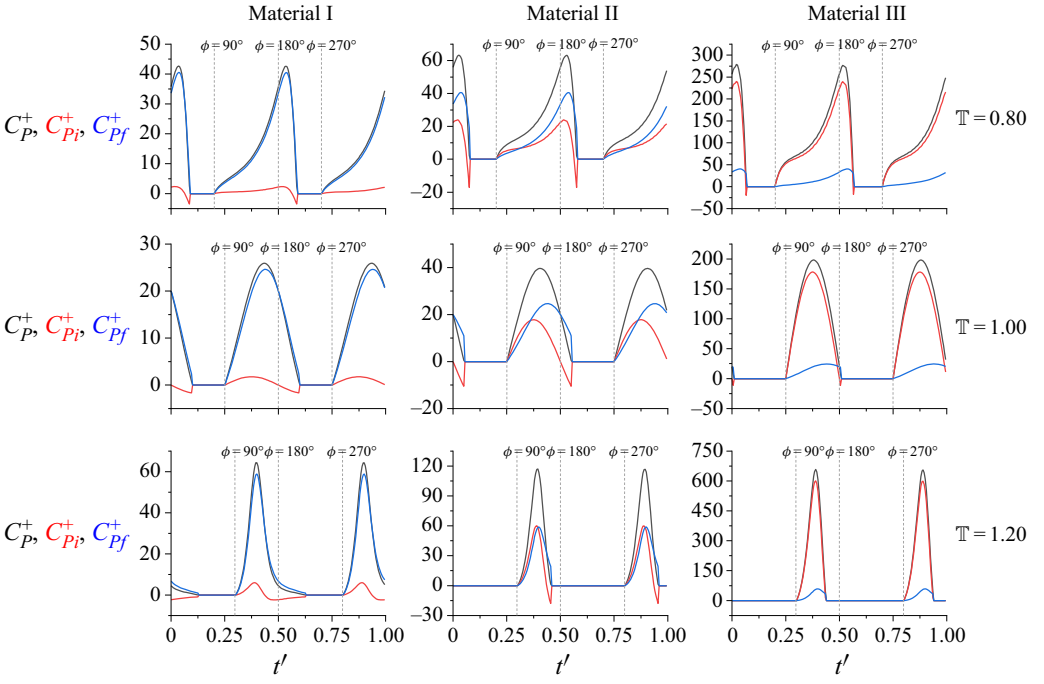

Figure 14. C_P^+ (black line), C_{Pf}^+ (blue line) and C_{Pi}^+ (red line) over a complete pitching cycle in the case of $St_A = 0.38$ for materials I (first column), II (second column) and III (third column), and for $\mathbb{T} = 0.80$ (first row), 1.00 (second row) and 1.20 (third row).

for $\mathbb{T} = 1.00$ and at $t' \approx 0.40$, 0.395 and 0.39 for $\mathbb{T} = 1.20$ (figure 14), which indicates that C_{Pi}^+ leads C_P^+, and C_P^+ leads C_{Pf}^+. It should be appreciated that C_{Pi}^+ could be negative whereas C_P^+ by definition is always positive or zero, thus a positive C_{Pf}^+ must accompany a negative C_{Pi}^+ such that $C_P^+ \geq 0$. A similar trend can be observed for $\mathbb{T} = 1.00$ and 1.20 in figures 14(*d–f*) and 14(*g–i*), respectively. The peak-to-peak phase difference between C_{Pi}^+ and C_P^+ decreases with the increase in the moment of inertia.

Figure 15 shows variations of $\bar{C}_{Pf}^+$, $\bar{C}_{Pi}^+$, $\bar{C}_P^+$ and η^+ in $\mathbb{T} - St_A$ plane for materials I, II and III in the left, middle and right columns, respectively. The variation of $\bar{C}_{Pf}^+$ is similar to that of $\bar{C}_P$. There are however two distinctions. First, $\bar{C}_{Pf}^+$ has a slightly larger magnitude than $\bar{C}_P$. Second, the minimum $\bar{C}_{Pf}^+$ for a given St_A occurs at $\mathbb{T} = 1.05$, 1.15, and 1.10 for materials I, II and III, respectively, while $\bar{C}_P$ is minimum at $\mathbb{T} = 1.00$ (figure 13*b*). The increase in the moment of inertia decreases $\bar{C}_{Pf}^+$, as can be seen by comparing the colours at any particular St_A and $\mathbb{T}$ in figure 15*a–c*). The $\bar{C}_{Pi}^+$ undoubtedly increases with increasing moment of inertia (see the colourmap ranges for figure 15*d–f*). The $\bar{C}_{Pi}^+$ first decreases with the increase in $\mathbb{T}$ from 0.80, reaches a minimum at $\mathbb{T} = 1.20$ for material I, and at $\mathbb{T} = 1.00$ for materials II and III, and then increases rapidly with further increase in $\mathbb{T}$. This implies that when $\bar{C}_{Pi}^+ \gtrsim \bar{C}_{Pf}^+$, $\bar{C}_{Pi}^+$ for the non-elastic system for a particular St_A will be minimum at $\mathbb{T} = 1.00$ (see figure 15*e,f*). The $\bar{C}_P^+$ for materials I and III follows the trends of $\bar{C}_{Pf}^+$ and $\bar{C}_{Pi}^+$, respectively, as $\bar{C}_{Pi}^+ \ll \bar{C}_{Pf}^+$ (making $\bar{C}_P^+ \approx \bar{C}_{Pf}^+$) for material I and $\bar{C}_{Pi}^+ \gg \bar{C}_{Pf}^+$ (making $\bar{C}_P^+ \approx \bar{C}_{Pi}^+$) for material III. For material II, because $\bar{C}_{Pi}^+ \approx \bar{C}_{Pf}^+$, $\bar{C}_P^+$ follows neither

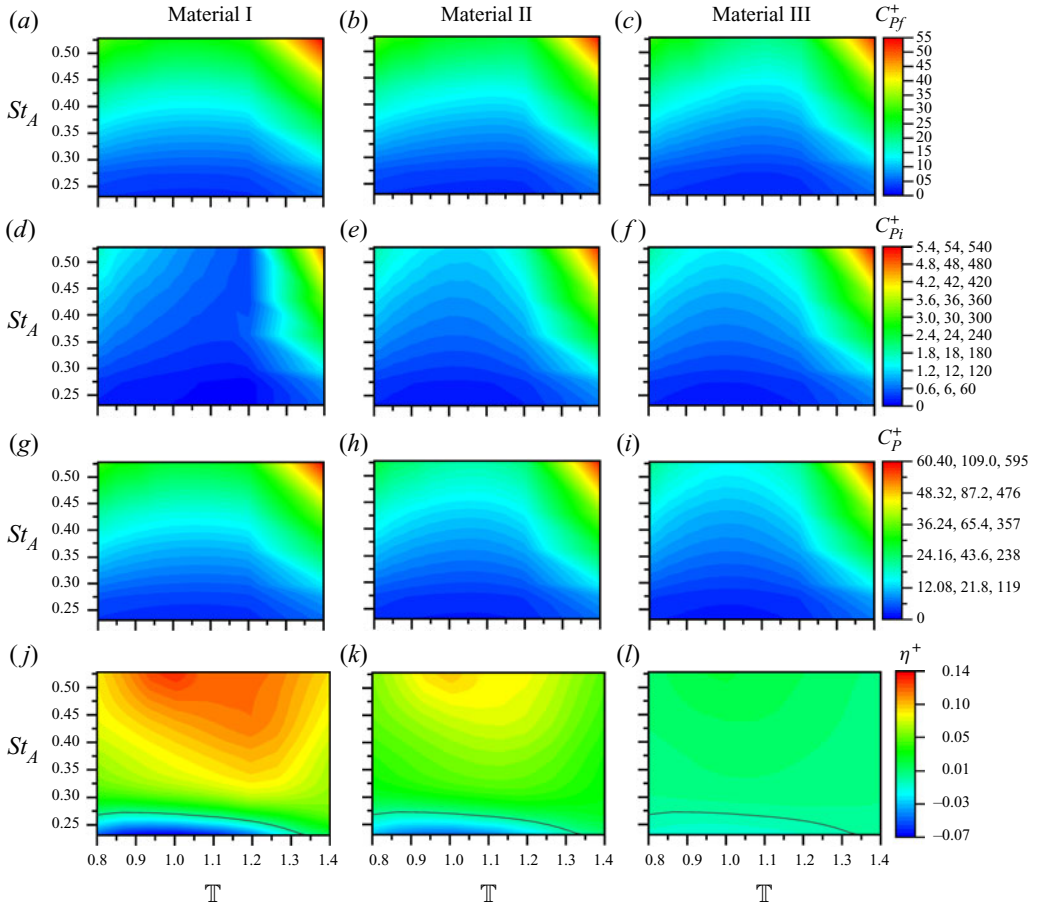

Figure 15. Variations of $\bar{C}_{Pf}^{+}$, $\bar{C}_{Pi}^{+}$, $\bar{C}_{P}^{+}$ and η^{+} in the $\mathbb{T} - St_A$ plane for materials I (left column), II (middle column) and III (right column). The colour code bars for $\bar{C}_{Pi}^{+}$ and $\bar{C}_{P}^{+}$ each have three scales for the three materials; left most, material I; middle, material II; and right most, material III. The black line in η^{+} maps corresponds to the drag–thrust transition.

$\bar{C}_{Pi}^{+}$ nor $\bar{C}_{Pf}^{+}$. The $\bar{C}_{P}^{+}$ decreases with $\mathbb{T}$ increasing from 0.80, becoming minimum at $\mathbb{T} = 1.05$ for materials I and II and at $\mathbb{T} = 1.00$ for material III, and then increases with a further increase in $\mathbb{T}$. The η^{+} for $0.30 < St_A \leq 0.45$ increases with $\mathbb{T}$ for $0.80 \leq \mathbb{T} \leq 1.20$, reaching a maximum at $\mathbb{T} = 1.20$, and then decreases with a further increase in $\mathbb{T}$ for $1.20 < \mathbb{T} \leq 1.40$. The η^{+} for $St_A > 0.45$, however, reaches its maximum at $\mathbb{T} = 1.00$. The variations of η^{+} in the $\mathbb{T} - St_A$ plane for materials II and III are similar to that for material I, except that the peak η^{+} along $\mathbb{T}$ axis for $0.30 < St_A < 0.45$ occurs at $\mathbb{T} = 1.10$ for material II and at $\mathbb{T} = 1.05$ for material III. For non-elastic storage systems, it can thus be concluded that the moment of inertia should be as low as possible, such that the inertial component of the power becomes negligible in comparison to the fluid power. Moreover, η^{+} can be enhanced with $1.05 < \mathbb{T} \leq 1.20$ for moderate St_A (i.e. $0.30 < St_A \leq 0.45$), while $\mathbb{T} = 1.00$ is beneficial in terms of η^{+} for $St_A > 0.45$.

The inertia does not affect $\bar{C}_P$ but plays an important role in determining $\bar{C}_{P}^{+}$. This is because $\bar{C}_{Pi}$ is always zero but $\bar{C}_{Pi}^{+}$ is positive, its magnitude increasing with increasing the

inertia of the foil (figure 15*d–f*). The effect of inertia is then reflected in efficiency with η^+ always smaller than η for the respective case. Because $\bar{C}_T$ is not affected by the inertia, the η^+ decreases with the increase in inertia as $\bar{C}_P^+ > \bar{C}_P$ i.e. $\bar{C}_{Pi}^+ > 0$.

3.5. *Effect of* $\mathbb{T}$ *on the wake structure*

Intuitively, an increase in pitching amplitude would result in a broader wake as the foil tip excursion is wide, whereas an increase in pitching frequency, owing to centrifugal force (Alam & Muhammad 2020), would increase the streamwise velocity in the wake. The focal parameter involved in this study is the kinematics (i.e. $\mathbb{T}$). Then, a question naturally arises, what is the effect of $\mathbb{T}$ on the wake? The answer to this question will be given here. Figure 13(*d*) shows the wake map for the $St_A - \mathbb{T}$ plane. There are only two basic wake patterns, namely 2S for $0.85 < \mathbb{T} \leq 1.40$ and 2P for $0.80 \leq \mathbb{T} \leq 0.85$, including their deflected patterns in small regions ($\mathbb{T} < 1.00$ for $St_A \geq 0.43$ and for $\mathbb{T} = 0.80$ only when $St_A = 0.42$. The wake deflection will be discussed in a separate section later. We will focus on 2P and 2S patterns only. Figure 16 illustrates the novel 2P wake pattern for $\mathbb{T} = 0.80$ and $St_A = 0.38$. The spanwise non-dimensional vorticity $\Omega_z^* (= \Omega_z d/U_\infty)$ snapshots are shown for $\phi = 90°$, 120°, …, and 0° in figure 16(*a–h*), overlapped with instantaneous relative streamwise velocity u_r^* ($= (u - U_\infty)/U_\infty$, dashed line) at a streamwise distance $x_{TE}^* (= x_{TE}/d) = 1.0$, where x_{TE} is measured from the foil tip at the equilibrium position. The u_r^* for the $\mathbb{T} = 1.00$ (solid line) is also shown as the baseline. For $\mathbb{T} = 0.80$, during the slower retract stroke ($\phi = 90°$–180°), a positive (counterclockwise) vortex A′ impinges along the lower surface, and another positive vortex A grows from the foil's tip (figure 16*a*,*b*). The formation of vortex A stems from the foil tip inertia (or can be said to arise from the flow separation at the tip) while that of vortex A′ originates from the flow separation at the leading edge. However, a negative vortex B′ originating from the leading edge impinges on the upper surface. During this slower retract stroke ($\phi = 90°$–180°, figure 16*a–d*), the tip vortex A grows and sheds above the wake centreline ($y^* = 0$) while the vortices A′ and B′ roll down over the lower and upper surfaces of the foil, respectively. The u_r^* strengthens around the wake centreline when the foil moves from $\phi = 90°$ to 180° while u_r^* around vortex A is negative (figure 16*c*,*d*).

The forward stroke ($\phi = 180°$–270°, figure 16*d–g*) is very fast (lowest $\mathbb{T} = 0.80$ examined), hence generating a very high acceleration. The foil tail thus leaves the wake centreline (equilibrium position) very fast, leaving vortex A above the wake centreline. This phenomenon is akin to the magic trick that when a sheet of paper on a table, with a coin on the top of the sheet, is pulled horizontally with a quick snap, the coin remains on the table, rather than moving with the paper. In the meanwhile, vortex A′ arriving at the foil tip reforms itself as the forward stroke is faster ($\phi = 180°$–270°, figure 16*d–g*). Vortex A′ lies abreast of vortex A, closer to the foil tip, merging with the braid shear-layer. Vortices A and A′ bundle together and form a paired vortex (figure 16*g*). Vortex A′, however, has a higher streamwise velocity than vortex A as A′ forms in the faster stroke (higher centrifugal force) and lies close to the wake centreline. The velocities of A and A′ could be understood from the corresponding u_r^* values around them. The return of the foil ($\phi = 270°$–0°, figure 16(*g*,*h*) further accelerates vortex A′. The merging line connecting A–A′ centres thus rotates anticlockwise, see the u_r^* profile and snapshots at $\phi = 270°$ and 0°. The same rotation signs of the individual vortices and of merging line facilitate the merging of the two vortices into one vortex in the next two strokes, which can also be seen from the evolution of the negative (blue coloured) paired vortices from $\phi = 180°$ to 0° (figure 16*d–h*). Similarly, vortex B forms as a tip inertia vortex from $\phi = 270°$

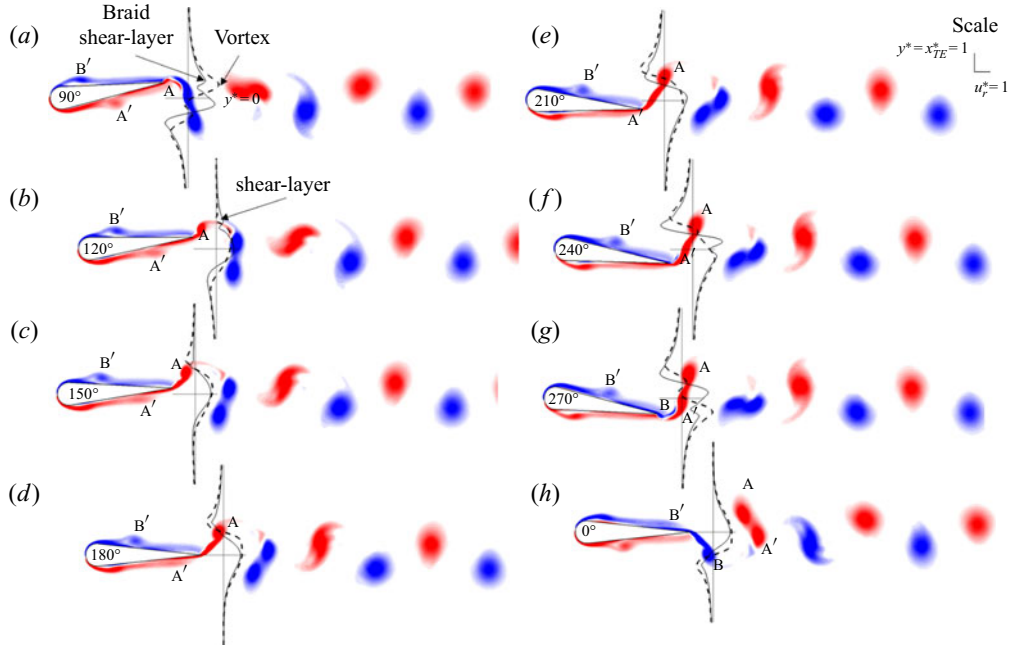

Figure 16. Contours of Ω_z^* showing generation and evolution of 2P wake ($St_A = 0.38$, $\mathbb{T} = 0.80$) at $\phi = 90°$, 120°, …, 270° in (*a–g*) and $\phi = 0°$ in (*h*). The $\Omega_z^* \in [-5, 5]$, with positive Ω_z^* shaded in red and negative Ω_z^* shaded in blue. The corresponding $u_r^* = (u - U_\infty)/U_\infty$ profiles (dashed line) are given at $x_{TE}^* = ((x - x_{TE})/d) = 1$. The solid line represents u_r^* for $\mathbb{T} = 1.00$. The horizontal and vertical lines represent $y^* = 0$ and $u_r^* = 0$, respectively.

to 0°. Overall, the paired vortices during their downstream evolution evolve into a single vortex in about two vortex-shedding cycles. The wake thus features 2P vortices up to $5d$ downstream from the foil tip and 2S vortices afterward.

There are several noticeable differences between the u_r^* profiles for $\mathbb{T} = 0.80$ and 1.00. First, at $\phi = 90°$ (figure 16*a*), the braid shear-layer for $\mathbb{T} = 1.00$ (figure 6*e*) is replaced by a vortex for $\mathbb{T} = 0.80$, as can be seen from higher u_r^* for $\mathbb{T} = 0.80$ than for $\mathbb{T} = 1.00$ above the wake centreline. When the foil moves from the upper extreme to the lower extreme, u_r^* at $y^* < 0$ (lower side of the wake) is greater for $\mathbb{T} = 0.80$ than for $\mathbb{T} = 1.00$ (figure 16*b–g*). Similarly, when the foil travels from the lower extreme to the upper (figure 16*g*,*h*), the u_r^* at $y^* < 0$ is enhanced for $\mathbb{T} = 0.80$.

The wake for $\mathbb{T} = 1.20$, however, is simply characterized by 2S vortices (figure 17), in a very similar fashion to that for $\mathbb{T} = 1.00$ (figure 6*c–f*). The tip vortex A rapidly grows from $\phi = 90°$ to 180° (faster stroke, figure 17*a–d*). Because of the faster foil rotation, vortex A is better concentrated and closer to the foil tip than its counterpart for $= 0.80$ in $\phi = 90°$ to 180° (slower stroke, see figure 16*a–d*). The leading-edge vortex A′ flattens and dies out when the foil travels from the upper extreme to the equilibrium. It further dies out in the forward stroke (figure 17*d–g*) and could not reach vortex A (figure 17*f*). It, however, contributes to vorticity in the braid shear-layer (figure 17*f*,*g*). The vortex A′ does not present itself in the wake. A single vortex is thus born in the wake when the foil travels from the upper extreme to the lower extreme. Similarly, another single vortex B comes into being when the foil returns to the upper extreme i.e. $\phi = 270°$ to 0° to 90° (figure 17*a*,*g*,*h*). Comparing the snapshots for $\phi = 180°$–270° between $\mathbb{T} = 0.80$ (figure 16*d–g*) and 1.20 (figure 17*d–g*), one can understand that vortex A′ for $\mathbb{T} = 0.80$ can reform itself in the

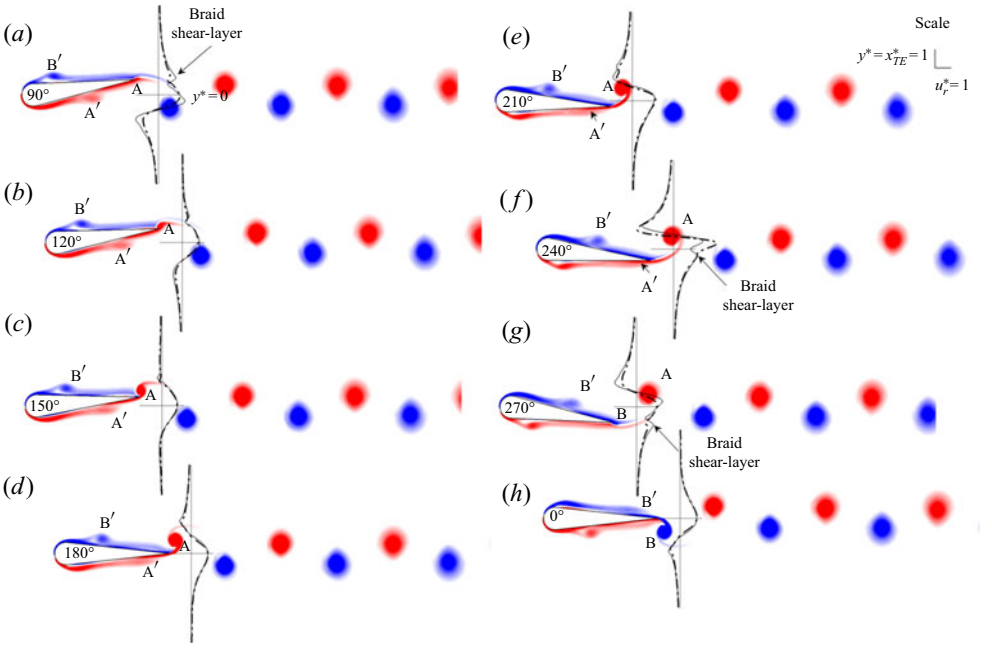

Figure 17. Contours of Ω_z^* showing generation and evolution of 2S wake ($St_A = 0.38$, $\mathbb{T} = 1.20$) at $\phi = 90°$, 120°, …, 270° in (*a–g*) and $\phi = 0°$ in (*h*). The $\Omega_z^* \in [-5, 5]$, with positive Ω_z^* shaded in red and negative Ω_z^* shaded in blue. The corresponding $u_r^* = (u - U_\infty)/U_\infty$ profiles (dashed line) are given at $x_{TE}^* = ((x - x_{TE})/d) = 1$. The solid line represents u_r^* for $\mathbb{T} = 1.00$. The horizontal and vertical lines represent $y^* = 0$ and $u_r^* = 0$, respectively.

wake, induced by the faster movement of foil tip (faster stroke) while that for $\mathbb{T} = 1.20$ cannot reform as the foil tip moves slowly. The u_r^* profile for $\mathbb{T} = 1.20$ closely mimics that for $\mathbb{T} = 1.00$ for most part of the cycle, except at $\phi = 210°$–$270°$ (just before reaching the extreme position). It can be seen that the vortex in the wake (e.g. vortex A in figure 17*f*) for $\mathbb{T} = 1.20$ is stronger than its counterpart for $\mathbb{T} = 1.00$, which accompanies a sudden burst of instantaneous u_r^*. Figure 18 shows wake structures for $St_A = 0.38$ at $\mathbb{T} = 1.40$, where the u_r^* profiles at $x_{TE}^* = 1$ for $\mathbb{T} = 1.00$ and 1.40 are overlaid onto the vorticity contours as solid and dashed lines, respectively. Like $\mathbb{T} = 1.20$, the $\mathbb{T} = 1.40$ also exhibits 2S wake, but with higher peak vorticity of the vortices (not shown). In addition, the vortices (e.g. A in figure 18*d*) form closer to the trailing edge when compared to the case of a smaller $\mathbb{T}$ (e.g. compare vortex A in figures 14*d*, 15*d* and 16*d*). The u_r^* profiles are qualitatively similar to those for $\mathbb{T} = 1.20$.

Indeed, observing the wake structures in the entire range of St_A and $\mathbb{T}$, we identified novel 2P reverse Kármán wake (figure 16), 2S reverse Kármán wake (figures 15 and 16) and asymmetric wake. The 2S Kármán or 2S aligned wake was not observed even at the lowest St_A ($= 0.23$) investigated here; this is in accordance with the wake map from the experimental work of Schnipper *et al.* (2009). The novel 2P reverse Kármán wake observed here is quite different from the 2P wake observed by Schnipper *et al.* (2009). The pairs observed in the present study have the same signed vortices such as A-A′, contrary to the opposite signed vortices (see figure 3 of Schnipper *et al.* 2009). Presently, the paired vortices form a single vortex downstream as having the same sign of vorticity. The paired vortices having different signs of vorticity do not merge, the wake appearing 2P far downstream (Schnipper *et al.* 2009).

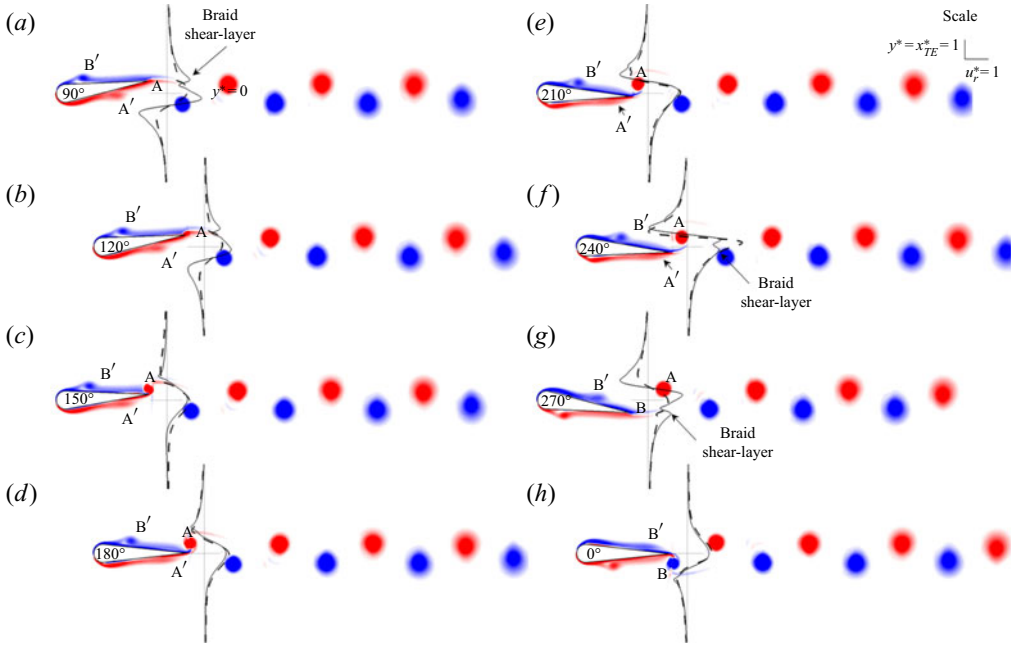

Figure 18. Contours of Ω_z^* showing generation and evolution of 2S wake ($St_A = 0.38$, $\mathbb{T} = 1.40$) at $\phi = 90°$, 120°, …, 270° in (*a–g*) and $\phi = 0°$ in (*h*). The $\Omega_z^* \in [-5, 5]$, with positive Ω_z^* shaded in red and negative Ω_z^* shaded in blue. The corresponding $u_r^* = (u - U_\infty)/U_\infty$ profiles (dashed line) are given at $x_{TE}^* = ((x - x_{TE})/d) = 1$. The solid line represents u_r^* for $\mathbb{T} = 1.00$. The horizontal and vertical lines represent $y^* = 0$ and $u_r^* = 0$, respectively.

The time-averaged streamwise $\bar{u}_r^*$ profiles in the wake for $\mathbb{T} = 0.80$, 1.00, 1.20 and 1.40 shown in figure 19 as dashed, continuous, dash–dotted line and dotted lines, respectively display that $\bar{u}_r^*$ is largely negative for $|y^*| = 0.65$–1.25 (depending on $\mathbb{T}$). This suggest a buffer (velocity deficit) zone between the wake jet (velocity excess) and the free stream, induced by the positive and negative vortices above and below the wake centreline. The $\bar{u}_r^*$ around the wake centreline is very high (e.g. at $x_{TE}^* = 1.00$; figure 19*a*), the maximum $\bar{u}_r^* = 0.82$, 1.05, 1.24 and 1.45 for $\mathbb{T} = 0.80$, 1.00, 1.20 and 1.40, respectively, i.e. the maximum averaged streamwise velocity reaches 182 %, 205 %, 224 % and 245 % of the freestream velocity, respectively, which indicates a jet-like flow. With the increase in $\mathbb{T}$, the $\bar{u}_r^*$ peak on the wake centreline extends at both x_{TE}^* values, while the wake width ($\bar{u}_r^* > 0$) narrows significantly at $x_{TE}^* = 1.00$ but negligibly at $x_{TE}^* = 6.00$ (figure 19*b*). The increased peak $\bar{u}_r^*$ with increasing $\mathbb{T}$ is, to some extent, linked to stronger vortices for the higher $\mathbb{T}$ (figure 18*f*).

Increasing A^* means increasing foil tip excursion; one thus expects an increased wake width. The flow centrifugal force arising from the foil rotation results from the maximum tip velocity that grows with increasing St_d or A^* or both (see (2.4)). The maximum tip velocity is thus connected to the streamwise velocity around the wake centreline. This raises a question, what is the effect of $\mathbb{T}$ on the wake width and wake velocity when changing $\mathbb{T}$ that changes neither A^* nor St_d? These simple intuitive arguments have not been addressed in the literature. We would like to shed some light on this point. Figure 20 shows the dependence of wake width w^* ($= w/d$) on the $\mathbb{T}$, A^* and St_d, where w is the jet width at $x_{TE}^* = 1.00$, defined by the cross-stream length for $\bar{u}_r^* > 0$. Figure 20(*a–c*) shows

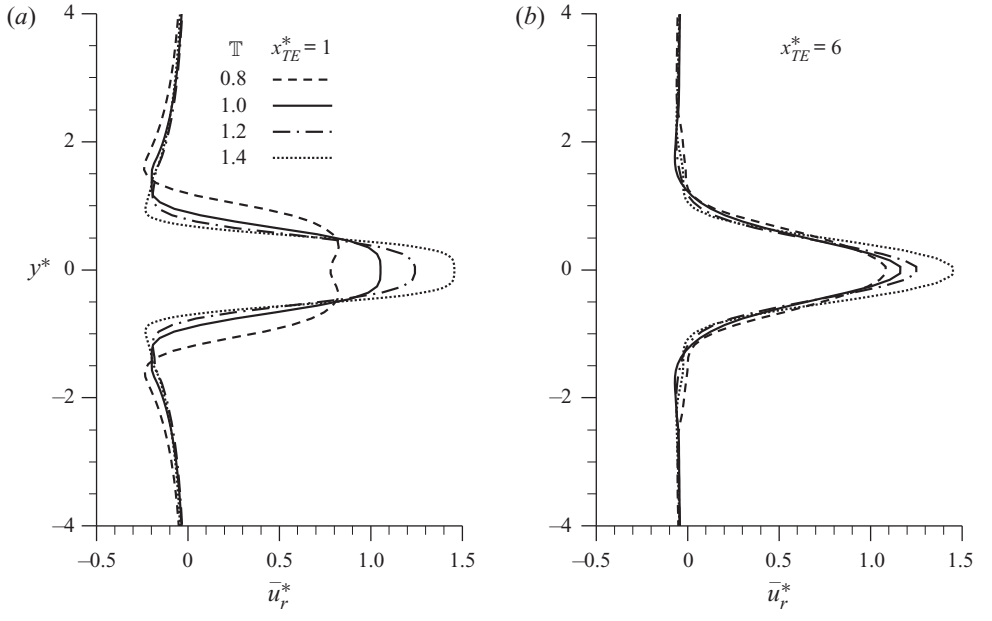

Figure 19. The cross-stream variation of non-dimensionalized time-average streamwise wake velocity ($\bar{u}^*_r = (\bar{u} - U_\infty)/U_\infty$) with $\mathbb{T}$ at (*a*) $x^*_{TE} = ((x - x_{TE})/d) = 1$ and (*b*) $x^*_{TE} = 6$ measured from the foil tip for $St_A = 0.38$.

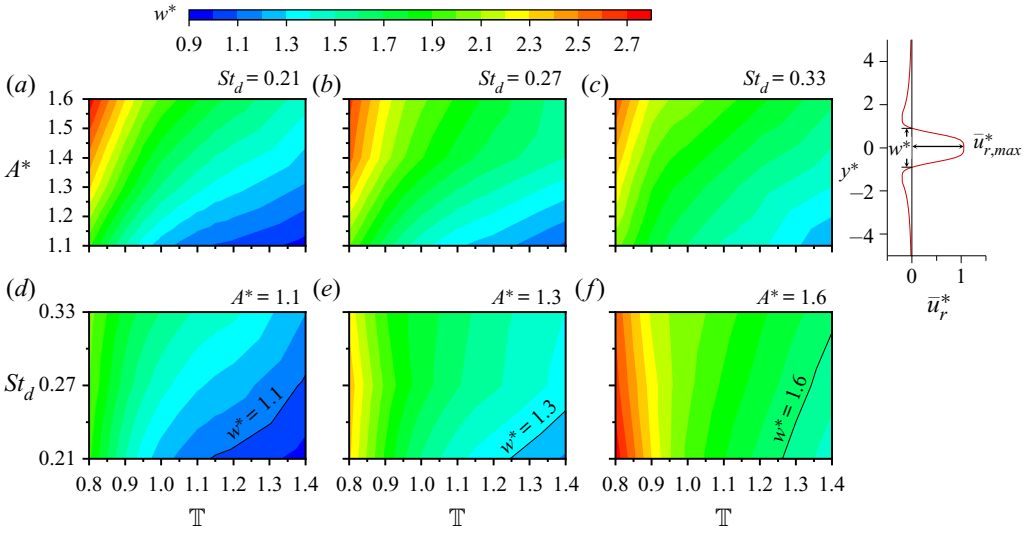

Figure 20. Contour maps of normalized wake width $w^* = (w/d)$ at $x^*_{TE} = 1$ for (*a*) $St_d = 0.21$, (*b*) $St_d = 0.27$, (*c*) $St_d = 0.33$, (*d*) $A^* = 1.1$, (*e*) $A^* = 1.3$ and (*f*) $A^* = 1.6$. The black contour lines in panels (*c*)–(*d*) show $w^* = A^*$.

the dependence of w^* on $\mathbb{T}$ and A^* at different St_d values, whereas figure 20(*d–f*) shows the same on $\mathbb{T}$ and St_d at different A^* values.

The w^* grows with increasing A^* for a given $\mathbb{T}$ but declines with increasing $\mathbb{T}$ for a given A^* (figure 20*a–c*). That is, the $\mathbb{T}$ effect on w^* is opposite to the A^* effect. The $\mathbb{T}$ effect on w^* although looking straightforward, a deeper explanation can be provided, which

Parameter	$\mathbb{T}$ increasing
$\bar{C}_T$	Decrease for $\mathbb{T} = 0.80 - 0.85$ and increase for $\mathbb{T} > 0.85$, minimum at $\mathbb{T} = 0.85$
$\bar{C}_P$	Decrease for $\mathbb{T} = 0.80 - 1.00$ and increase for $\mathbb{T} > 1.00$, minimum at $\mathbb{T} = 1.00$
η	Increase for $St_A = 0.3$–0.4, reaching maximum at $\mathbb{T} = 1.0$ for $St_A > 0.5$;
η	decrease and increase in the drag regime, minimum at $\mathbb{T} = 0.90$
w^*	Exponential decrease
$\bar{u}^*_{r,max}$	Increase

Table 2. Effect of $\mathbb{T}$ on $\bar{C}_T$, $\bar{C}_P$, η, w^*, and $\bar{u}^*_{r,max}$.

links with fluid angular momentum that is essentially a representation of C_{Pf}. Indeed, the forward stroke is more connected to w^* than the retract stroke as the forward stroke diverges fluid away from the wake centreline while the retract stroke brings fluid toward the wake centreline, albeit not at the same scale. For $\mathbb{T} = 1.00$, the angular momentum varies similarly in the forward and retract strokes (figure 6*a*). When $\mathbb{T}$ is decreased from 1.00, the faster forward stroke causes a large variation in C_{Pf} in the forward stroke (figure 8*a*), diverging the fluid away from the wake centreline with a large angular momentum. The w^* thus widens with decreasing $\mathbb{T}$ from 1.00. In contrast, when $\mathbb{T}$ is increased from 1.00, the forward stroke becomes slower and has a smaller variation in C_{Pf} than the retract stroke (figures 7*a* and 8*a*). The smaller angular momentum during the forward stroke thus corresponds to a narrower w^*. Another feature is that the decrease in w^* with increasing $\mathbb{T}$ is not linear, rather faster at lower $\mathbb{T}$, as can be observed from steeper slopes of the contour lines at lower $\mathbb{T}$ (figure 20*a–c*). At a constant A^*, the w^* boosts with increasing St_d particularly for $\mathbb{T} > 1.00$ (figure 20*d–e*) as a higher oscillation frequency produces more angular momentum. The effect of St_d on w^*, however, diminishes with increasing A^* (figure 20*d–f*). The peak-to-peak amplitude A^* instead of the half-amplitude is adopted in most of the literature as it is assumed to represent wake width as well. A scrupulous observation on w^* contours suggests that w^* is larger than A^* for $\mathbb{T} = 1.00$ and is also a function of St_d (see figure 20*d–f*).

The jet produced in the wake is expected to be highly connected to $\bar{C}_T$. The maximum jet velocity in the wake is a measure of the jet strength. It is worth studying the dependence of jet velocity on A^*, $\mathbb{T}$ and St_d. We measured the maximum jet velocity as the maximum time-average streamwise velocity $\bar{u}^*_{r,max}(= max(\bar{u}^*_r))$ at $x^*_{TE} = 1.00$. The dependence of $\bar{u}^*_{r,max}$ can be understood from the contour plots of $\bar{u}^*_{r,max}$ on the $A^* - \mathbb{T}$ and $St_d - \mathbb{T}$ planes in figure 21. An increase in $\mathbb{T}$ and/or A^* results in a monotonic increase in $\bar{u}^*_{r,max}$ (figure 21*a–c*). This is consistent with the fact that $\bar{C}_T$ enhances with increasing $\mathbb{T}$ and/or A^*. At a given $\mathbb{T}$, an increase in St_d leads to an increased $\bar{u}^*_{r,max}$ (figure 21*d–f*). Overall, increasing $\mathbb{T}$ from 1.00 strengthens the jet (increasing $\bar{u}^*_{r,max}$), which narrows the w^*, whereas decreasing $\mathbb{T}$ from 1.00 widens the jet (increasing w^*), which weakens the jet. It is worth noting that the jet characteristics can be modified by changing $\mathbb{T}$ only for constant St_d and A^*. For a sinusoidal pitching foil, increasing A^* is capable of both strengthening and widening the jet. However, increasing St_d largely fortifies the jet, with negligible influence on the jet width. The effects of $\mathbb{T}$ on St_d, A^*, St_A, $\bar{C}_T$, $\bar{C}_P$, w, and $\bar{u}^*_{r,max}$ are summarized in table 2.

When $\mathbb{T}$ is increased from 0.80 to 1.40, both $\bar{C}_T$ and $\bar{C}_P$ first decrease and then increase, having minimum at $\mathbb{T} = 0.85$ and 1.00, respectively. However, η for $0.3 < St_A < 0.4$

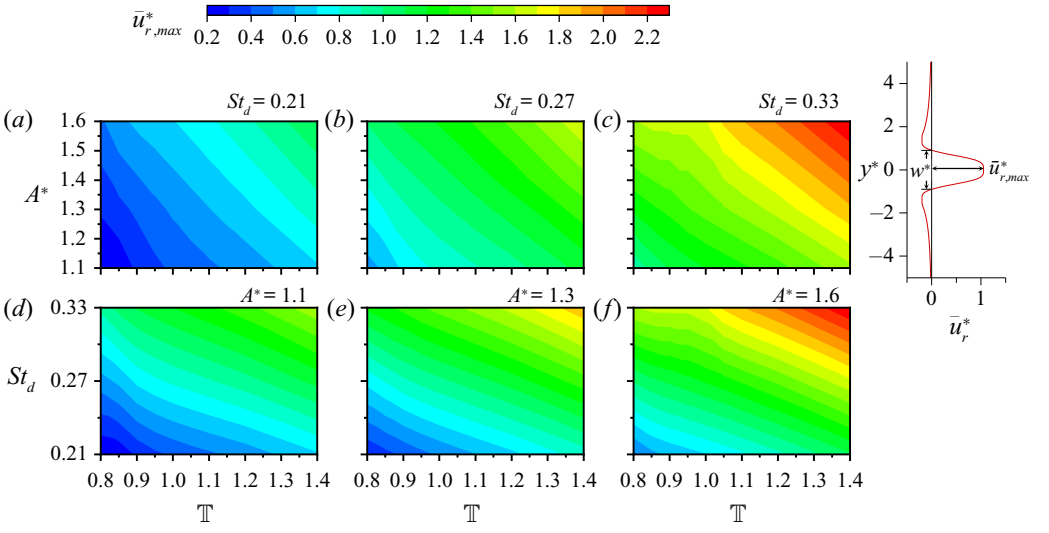

Figure 21. Contour maps of normalized maximum wake velocity $\bar{u}^*_{r,max}$ at $x^*_{TE} = 1$ for (*a*) $St_d = 0.21$, (*b*) $St_d = 0.27$, (*c*) $St_d = 0.33$, (*d*) $A^* = 1.1$, (*e*) $A^* = 1.3$ and (*f*) $A^* = 1.6$.

Parameter	St_d increasing	A^* increasing	St_A increasing
$\bar{C}_T$	Exponential increase	Exponential increase	Exponential increase
$\bar{C}_P$	Exponential increase	Exponential increase	Exponential increase
η	Logarithmic increase	Logarithmic increase	Logarithmic increase
w^*	Decrease ($0.80 \leq \mathbb{T} < 0.90$)	Linear increase	Constant St_d
	Increase ($0.90 < \mathbb{T} \leq 1.40$)		Linear increase
			Constant A^*
			Decrease ($0.80 \leq \mathbb{T} < 0.90$)
			Increase ($0.90 < \mathbb{T} \leq 1.40$)
$\bar{u}^*_{r,max}$	Linear increase	Linear increase	Linear increase

Table 3. Effect of St_d, A^* and St_A on $\bar{C}_T$, $\bar{C}_P$, η, w^* and $\bar{u}^*_{r,max}$.

increases monotonically with $\mathbb{T}$ while that for $St_A > 0.4$ first increases and then decreases with $\mathbb{T}$. For the drag regime, η has a minimum at $\mathbb{T} = 0.90$, with η decreasing and increasing for $0.80 \leq \mathbb{T} < 0.90$ and $0.90 < \mathbb{T} \leq 1.40$, respectively (table 2). The w^*, however, monotonically declines and $\bar{u}^*_{r,max}$ grows with increasing $\mathbb{T}$. The parameters St_d, A^* and St_A are linked to one another in a fashion of $St_A = St_d \times A^*$. Hence, a change in St_d and/or A^* modifies St_A. When St_A is increased by increasing St_d or A^*, the $\bar{C}_T$ and $\bar{C}_P$ increase exponentially and $\bar{u}^*_{r,max}$ increases linearly. The w^* increases with St_A if St_d is held constant and if A^* is constant, then w^* decreases with St_A from $0.80 \leq \mathbb{T} < 0.90$ and it increases with St_A for $0.90 < \mathbb{T} \leq 1.40$ (table 3).

3.5.1. *Deflected wakes and* $\mathbb{T}$ *effect on wake asymmetry*

The deflected (asymmetric) wake was found at small $\mathbb{T}$ and large St_A, as seen in figure 13(*d*) (upper-left corner). The averaged wake jet deflection angle θ_w was measured by a linear fit of the cross-stream position of $\bar{u}^*_{r,max}$ in the near wake ($1 \leq x^*_{TE} \leq 10$)

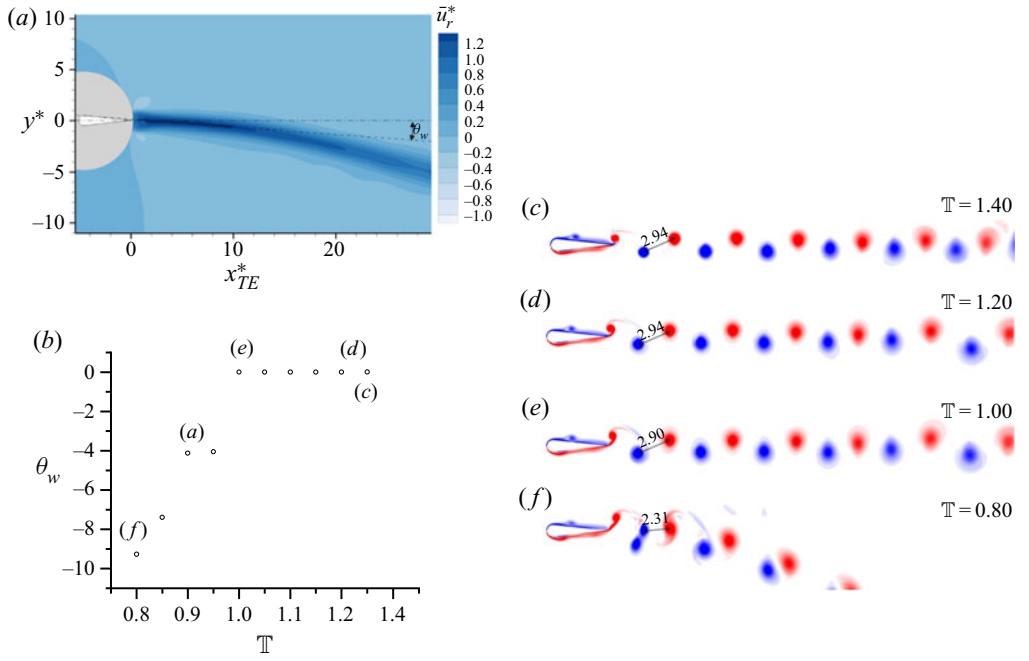

Figure 22. (*a*) The wake deflection angle measured by linear fit of maximum wake velocity points (circles) in near wake (for $\mathbb{T} = 0.80$, $St_A = 0.432$), dash–dotted line and dashed line depict $y^* = 0$ and least square fit for the near wake deflection angle ($1 \leq x_{TE}^* \leq 10$). (*b*) The wake deflection angle against $\mathbb{T}$. Vorticity contours for $\mathbb{T} = 1.40$, 1.20, 1.00, and 0.80 in (*c*), (*d*), (*e*) and (*f*), respectively. All data in panels (*a–f*) are for $St_A = 0.432$.

as shown in figure 22(*a*). This method of estimating θ_w was proposed by Godoy-Diana *et al.* (2009). The θ_w for $St_A = 0.43$ against $\mathbb{T}$ is shown in figure 22(*b*). The negative value of θ_w indicates the wake deflecting downward. The wake is symmetric for $\mathbb{T} = 1.00 - 1.40$ (i.e. $\theta_w = 0°$) and becomes asymmetric when $\mathbb{T}$ is decreased from 1.00, $\theta_w = -9.3°$ at the lowest $\mathbb{T}$ ($= 0.80$) examined. As shown in figure 13(*d*), at $St_A = 0.429$, asymmetric wake is only seen at $\mathbb{T} = 0.80$, however, when the St_A is increased slightly (i.e. $St_A = 0.432$), the asymmetric wake appears at higher $\mathbb{T}$ ($0.80 \leq \mathbb{T} < 1.00$, see figure 13*d*). The metamorphosis of the symmetric wake into the deflected wake at $\mathbb{T} < 1.00$ arises from the slower retract stroke generating vortices further away from the foil tip (e.g. compare vortex A in figure 16*d* to that in figure 17*d*). Thus, the distance between the two completely shed nearest counter-rotating vortices in the near wake shrinks. For example, vortices A′ and B in figure 16(*h*) ($\mathbb{T} = 0.80$) are closer to each other than vortices A and B in figure 17(*h*) ($\mathbb{T} = 1.20$). This makes them susceptible to forming a dipole vortex pair with a vortex of the opposite sign of rotation shed in the previous half-cycle. The formation of the vortex pair triggers the wake asymmetry (Marais *et al.* 2012). This is clearly depicted in figure 22(*c–f*) where the vorticity contours behind the foil pitching for $\mathbb{T} = 1.40$, 1.20, 1.00 and 0.80 are shown, respectively. The distance (normalized with d) between the first two completely shed vortices (opposite signed) is measured and marked in figure 22(*c–e*). The distance is measured between the locations of maximum and minimum vorticities. It can be seen that a decrease in $\mathbb{T}(0.80 \leq \mathbb{T} \leq 1.20)$ is accompanied by decreasing distance between two opposite sign vortices, which leads to increasing the chance for the asymmetric wake formation.

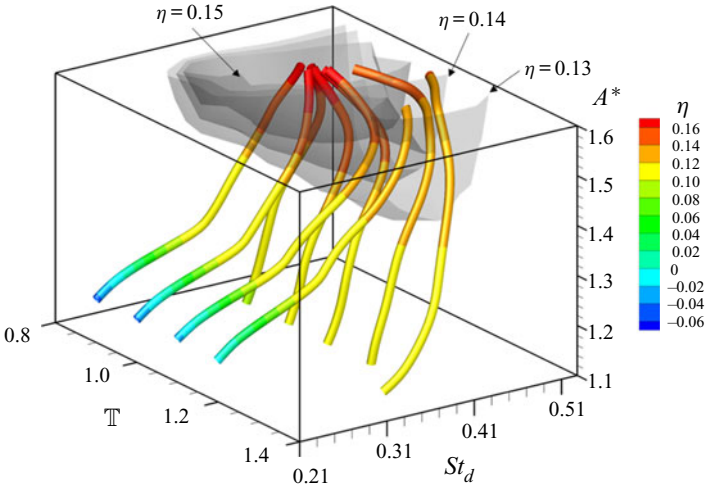

Figure 23. The steepest ascent curves coloured with efficiency, with the iso-contour (grey surfaces) showing three levels of η.

3.6. *Discussion*

Here, we pay attention to the origin of thrust and the effect of $\mathbb{T}$ on it. The St_A will thus be assumed constant for this discussion. As discussed by Alam & Muhammad (2020), the $\dot{\theta}$ and $\ddot{\theta}$ have a strong correlation with forces (surface pressure) and moments on the foil, while the qualitative vortex structure does not change much. The averaged forces and moments on a foil, however, do correlate to the averaged flow field in the wake. There are a few interesting points on the effect of $\mathbb{T}$ on thrust and wake flow, where physical insight into them should be explored. For example, why does the wake widen with decreasing $\mathbb{T}$? Why is thrust robust at a high $\mathbb{T}$?

The momentum balance in the streamwise direction does point out the wake relation to (average) thrust. As mentioned in the introduction, the streamwise momentum balance over-estimates thrust. The underlying cause is that pitching motion is purely a rotational motion, which induces the rotational motion of the fluid surrounding the foil and the generation of streamwise momentum of fluid is a reaction of rotational motion of the foil on fluid. The correlation between average thrust and jet wake thus gives rise to the *post hoc ergo propter hoc* fallacy, whereby an assumption is made that thrust is the reaction of streamwise jet and *vice versa*. In this case, correlation does not imply causation. They (thrust and jet wake) are essentially inter-dependent and contingent on the angular motion of the foil. Naturally, we then need to understand the relationship of the foil motion (θ, $\dot{\theta}$, $\ddot{\theta}$) to thrust and wake. The C_T and wake characteristics (such as u_r^*) should follow the respective $\dot{\theta}$ that produces a centrifugal jet owing to the centrifugal acceleration (Alam & Muhammad (2020).

The $\dot{\theta}$ profile for $\mathbb{T} < 1.00$ and $\mathbb{T} > 1.00$ are mirror images of each other (see e.g. $\mathbb{T} = 0.80$ and 1.20 in figure 3*b*) while the difference in $\bar{C}_T$ for $\mathbb{T} < 1.00$ and $\mathbb{T} > 1.00$ (see e.g. figure 5*a*,*i*) can be understood by the phenomenon of the resonance between natural ($\mathbb{T} = 1.00$) vortex shedding and modified motion ($\mathbb{T}$) vortex shedding. During the natural vortex shedding ($\mathbb{T} = 1.00$, figure 6*c*–*f*), most of the tip shear-layer roll-up occurs in the retract stroke. By speeding up the retract stroke for $\mathbb{T} > 1.00$, a resonance is created between the natural tip shear-layer roll-up and the increased $\dot{\theta}$ of the foil. Hence, a stronger jet is formed behind the foil with $\mathbb{T} > 1.00$ accompanying higher $\bar{C}_T$. When $\mathbb{T}$ is decreased from 1.00,

the tip shear-layer roll-up process slows down in the slower retract stroke and speeds up in the faster forward stroke. The slower retract stroke causes a decreased $\bar{u}_r^*$ owing to the slowed roll-up of the shear layer at the tip of the foil, while the fast forward stroke not only adds additional vorticity to the tip shear-layer but also flings the flow outward (away from the symmetry) and hence increases w^*. Thus, the loss of $\bar{C}_T$ arising from weaker tip shear-layer roll-up in the retract stroke (for $\mathbb{T} = 0.80$) is compensated by the increased w^* and stronger tip-shear-layer roll-up in the faster forward stroke. There is a net decrease in $\bar{C}_T$ with $\mathbb{T}$ for $\mathbb{T} < 1.00$ until $\mathbb{T} = 0.85$ (figure 12*a*), where the increased shear-layer contribution in the forward stroke enhances and creates an additional vortex (such as A′ in figure 16). This additional vortex is accompanied by increased w^* that compensates for the loss of jet velocity; thus $\bar{C}_T$ starts increasing for $\mathbb{T} < 0.85$. The $\bar{C}_P$ is higher for $\mathbb{T} > 1.00$ than for $\mathbb{T} < 1.00$, but owing to resonance in the natural vortex shedding process and induced vortex shedding, η for $\mathbb{T} > 1.00$ is higher than that for $\mathbb{T} < 1.00$ (for a constant $St_A > 0.30$). To quantify the increase or decrease of the tip shear-layer roll-up contribution, we measured the circulation of the shed vortices by integrating the vorticity times the area. Visual inspection of the wake from figures 6(*c–f*), 14, 15 and 16, showed that most of the lower surface shear-layer roll-up behind the foil tip occurs between phase 90°–180° (i.e. from the extreme position to the equilibrium position). The circulation around the vortex A or A–A′ (whichever the case may be) at $\phi = 180°$ (figures 14–16) was 64 %, 76 %, 89 % and 99 % of the circulation about the same vortex A or A-A′ at $\phi = 270°$, for $\mathbb{T} = 0.80$, 1.00, 1.20 and 1.40, respectively. This shows that the contribution of the shear-layer to the shed vorticity for the forward stroke ($\phi = 180°$ to 270°) becomes higher with decreasing $\mathbb{T}$. For the sinusoidal motion, 76 % of the shear-layer roll-up (on one side of the foil, during a cycle) is done in the retract stroke ($\phi = 90°$ to 180°). The speeding up of the retract stroke ($\mathbb{T} > 1.00$) resonates with the natural cycle of the shear-layer roll-up process (i.e. for $\mathbb{T} = 1.00$), thus the $\bar{C}_T$ and η are both reinforced as compared to those from $\mathbb{T} = 1.00$ (figure 12*a*,*c*). Conversely, for $\mathbb{T} < 1.00$, the natural roll-up process (i.e. like that for $\mathbb{T} = 1.00$) is disturbed, thus we see a decrease in $\bar{C}_T$ and η for $\mathbb{T} < 1.00$, except for $\mathbb{T} = 0.80$ (figure 12*a*,*c*), where the shear-layer roll-up process gets in tune with the kinematics again and a much stronger A′ vortex starts shedding in the wake in the forward stroke (figure 16*d–g*), which compensates for the weakened tip vortex (e.g. vortex A) enough to gain additional thrust.

The St_d and A^* ranges of the current study do not contain the optimal St_d and A^* combination for peak thrust. Nevertheless, in this sub-optimal range of parameters, we do get thrust and efficiency enhancements by altering the kinematics of the pitching foil. From the literature, we know the efficiency has a single maximum in the St_d–A^* plane (Triantafyllou *et al.* 1991, 1993; Mackowski & Williamson 2015). This means that if all the maxima of peak efficiency in the St_d–A^* plane are joined with a line, it could show us the optimal efficiency in the three-parameter study undertaken here. Because the line of maxima is outside the studied ranges of parameters, we plotted the steepest ascent lines for the efficiency enhancement in figure 23. The steepest ascent lines are the streamlines of the gradient field with respect to the input parameters, i.e. $\nabla\eta = (\partial\eta/\partial\mathbb{T}, \partial\eta/\partial St_d, \partial\eta/\partial A^*)$. The steepest ascent lines lead to the global optimum and indicate the response sensitivity (for more details see Fernex *et al.* 2020). The steepest ascent lines seem to converge at $\mathbb{T} = 1.00$, $A^* = 1.6$ and $St_d \approx 0.4$. The optimal St_d decreases with increasing A^*. The St_A corresponding to the optimum η is ≈ 0.63 that is within the range of natural swimmers (see A2 for details). The figure further demonstrates that at large St_A, beyond the maximum η, the flow becomes chaotic, as such the enhancement of η and $\bar{C}_T$ does not hold anymore.

The $\mathbb{T} > 1.00$ at large St_A (>0.5) is thus not effective anymore in terms of η. This however does not undermine the importance of employing $\mathbb{T}$ for lower St_A as the fish and marine animals do not always swim at optimum efficiency.

4. Conclusions

The previous works on foil with different modified pitching motion reported either enhanced thrust or enhanced efficiency, which revealed the necessity to find a way to enhance both thrust and efficiency simultaneously. Here we have introduced a novel modified pitching motion inspired by nature and investigated the hydrodynamics of a foil undergoing the novel modified pitching motion. The novel pitching motion includes a variation in the time period ratio $\mathbb{T}$ in [0.80, 1.40], featuring a competition between the foil speeds in forward and retract strokes, with $\mathbb{T} > 1.00$ giving the faster retract stroke than the forward stroke and *vice versa* with $\mathbb{T} < 1.00$. The St_d (= 0.21–0.33) and A^* (= 1.1–1.6) of the pitching foil have also been varied to show the benefit of the modified pitching motion over the range of operating conditions.

The relationship between C_T and C_P changes substantially with $\mathbb{T}$. A decrease in $\mathbb{T}$ from 1.00 to 0.80 makes the C_T and C_P peaks move away from each other, almost out of phase at $\mathbb{T} = 0.80$ where the C_T peak coincides with the C_P valley and *vice versa*. Increasing $\mathbb{T}$ from 1.00 to 1.40 causes the C_T and C_P peaks to move towards each other so that they are almost in-phase at $\mathbb{T} = 1.40$. The characteristics and results of $\mathbb{T} > 1.00$ motions in the faster stroke bear a resemblance to the fast start of a prey fish to escape while those of $\mathbb{T} < 1.00$ correspond to the braking locomoton for fish swimming.

An increase in $\mathbb{T}$ from 1.00 enhances $\bar{C}_T$, $\bar{C}_P$ and η, for example by 25.2 %, 14.5 % and 8.5 % at $\mathbb{T} = 1.20$, and by 105 %, 86 % and 10 % at $\mathbb{T} = 1.40$ with $St_A = 0.38$. The enhancement is attributed to the synchronization between the natural vortex shedding ($\mathbb{T} = 1.00$) and the contribution of modified pitching motion to the vortex shedding, with the retract stroke making the vortices faster and stronger. As a result, the wake width shrinks and the maximum jet velocity increases in the wake. Larger $\bar{C}_P$ is required when $\mathbb{T}$ is increased from 1.00 as an increased speed of pitching undergoes an increased flow resistance. For $St_A > 0.4$, the η increases for $0.80 \leq \mathbb{T} \leq 1.20$ and decreases for $\mathbb{T} > 1.20$. With a further increase in St_A (>0.5), the η peaks at $\mathbb{T} = 1.00$. A decrease in $\mathbb{T}$ from 1.00 also requires higher $\bar{C}_P$ for the same reason, as the only difference between $\mathbb{T} > 1.00$ and $T < 1.00$ is the faster and slower strokes swapping with each other. The $\bar{C}_P$ is minimum at $\mathbb{T} = 1.00$ while $\bar{C}_T$ is at $\mathbb{T} = 0.85$. A 2P wake is observed for $\mathbb{T} \leq 0.85$, which shares the boundaries with the minimum $\bar{C}_P$.

The $\bar{C}_{Pi}$ is always zero while $\bar{C}^+_{Pi}$ is always greater than zero. This is because for perfectly elastic energy storage systems, $C_{Pi} > 0$ and $C_{Pi} < 0$ cancel each other; however, $C_P < 0$ cannot be used for non-elastic energy storage systems. The $\bar{C}^+_{Pi}$ increases with increasing foil inertia. The $\bar{C}^+_{Pf}$ and $\bar{C}^+_P$ are both larger than $\bar{C}_{Pf}$ and $\bar{C}_P$, respectively, thus making η^+ to be smaller than η for the same case. The η^+ drops with increasing $\mathbb{T}$ for $\mathbb{T} > 1.20$ at $0.30 < St_A \leq 0.45$ and for $\mathbb{T} > 1.00$ at $St_A > 0.45$ owing to sufficiently large $\bar{C}^+_{Pi}$.

The wake deflection is not seen for $\mathbb{T} = 1.00$ for $St_A < 0.4$ (Godoy-Diana *et al.* 2008, 2009; Alam & Muhammad 2020). However, the wake deflects for the high St_A examined when $\mathbb{T}$ is decreased from 1.00, e.g. at $St_A = 0.429$, $\mathbb{T} = 0.80$; $St_A = 0.432$, $0.80 \leq \mathbb{T} < 1.00$. That is, a smaller $\mathbb{T}$ sets off a deflected wake, reducing the distance between two oppositely signed vortices in the near wake. However, a higher $\mathbb{T}$ suppresses the wake

deflection, widening the distance between the two oppositely signed vortices in the near wake.

Four swimming regimes are discussed: undesirable ($C_T < 0;\ C_P > 0$), floating ($C_T < 0;\ C_P < 0$), normal ($C_T > 0;\ C_P > 0$) and ideal ($C_T > 0;\ C_P < 0$). The undesirable and normal swimming regimes are power hungry (i.e. $C_P > 0$), while the other two are power generating (i.e. $C_P < 0$). The forward stroke consists of undesirable, floating and ideal regimes, while the retract stroke consists of normal swimming and some part of the undesirable regime for all $\mathbb{T}$. An increase in $\mathbb{T}$ expands the undesirable and floating regimes, both having $C_T < 0$, in the forward stroke and hence decreases $\bar{C}_{TF}$. Although the faster retract stroke with increasing $\mathbb{T}$ does not affect the span of the normal swimming ($C_T > 0$) and undesirable ($C_T < 0$) regimes, the magnitude of C_T does grow rapidly in the normal swimming regime, largely contributed by $\bar{C}_{TR}$.

The thrust and power response for the kinematics with $\mathbb{T} > 1.00$ (e.g. $\mathbb{T} = 1.20$ and 1.40) correspond to fast start locomotion where the largest thrust is generated in-phase with the input power with a high lateral force near the extreme position. The steady swimming gate is connected to sinusoidal pitching ($\mathbb{T} = 1.00$), where a steady motion of the tail guarantees thrust to sustain steady swimming. A small $\mathbb{T}$ (e.g. $\mathbb{T} = 0.80$) imitates braking locomotion where the power is required to generate drag to stop the forward motion, with C_T and C_P being out of phase.

The equations of motion ((2.2)–(2.5)) are implicit and somewhat complicated, which could be simplified and written in an explicit formulation using optimization techniques. It would be interesting to apply the novel asymmetric motion to heaving and heaving + pitching foils.

Funding. The authors wish to acknowledge the support given by the National Natural Science Foundation of China through Grants 12172109, 11672096 and 91752112 and by Research Grant Council of Shenzhen Government through grant JCYJ20180306171921088.

Declaration of interests. The authors report no conflict of interest.

Author ORCIDs.
Zaka Muhammad http://orcid.org/0000-0002-9279-7613;
Md. Mahbub Alam http://orcid.org/0000-0001-7937-8556;
Bernd R. Noack http://orcid.org/0000-0001-5935-1962.

Appendix

A.1. *Range of* $\mathbb{T}$

The modified waveform shown in figure 2(*c*) has slope discontinuities at $t = 0$, $T/2$ and T. To make the proposed quasi-symmetric motion continuous and differentiable, we need to make sure that the slope (first derivative) of the motion is continuous at the stroke crossover (i.e. at the end and start of each stroke). To achieve this objective, one could use a blending function to smooth the motion trajectory at each stroke crossover, but the blending function would add additional parameters to the problem. We changed the motion by stretching and contracting the time axis (l') for a sinusoidal waveform to create the proposed motion without any discontinuity. The idea of compressing / stretching of the time axis follows the curved time–space concept (Wald 2010). Equation (2.3) modifies the time by stretching / compressing between intervals (0, 0.5) and (0.5, 1) of t', which results in a waveform with constant slope at $t' = 0$, 0.5 and 1. Although the formulation derived in (2.4) is continuously differentiable, it poses a limit on $\mathbb{T}$.

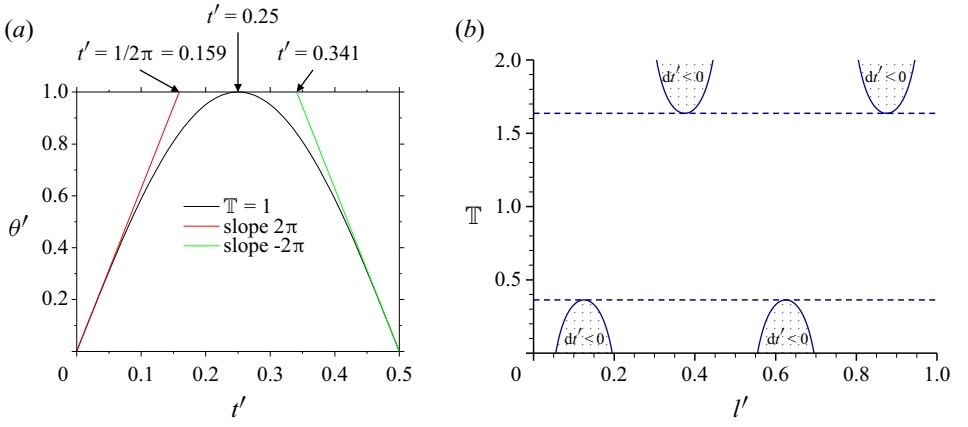

Figure 24. The limitation of $\mathbb{T}$, shown (*a*) as a geometrical constraint (red and green lines) posed by slope, (*b*) as the contour plot of $\mathrm{d}t'$ on the $l' - \mathbb{T}$ plane. The constraint positive finite slope ($\mathrm{d}t' < 0$) is shown by the dotted region.

The limitation can be geometrically estimated as shown in figure 24(*a*), where the first half of the oscillation cycle for $\mathbb{T} = 1.0$ is shown as the black line while the constraints of the continuous and constant slope at stroke crossover (i.e. at $t' = 0$ and 0.5) are shown with red and green lines. The motion is manipulated by moving the peak, that is at $t' = 0.25$ for $\mathbb{T} = 1.0$, to the left or right. Because of the constant slope constraint of $\pm 2\pi$ at $t' = 0$ and 0.5, respectively, the peak can move only to the extent ($t' = 0.159$ and 0.341) shown by the constant slope lines.

The mathematical way of finding the limits is to check for function $\theta'(t)$. To be a valid function, there should be only one value of θ' at a given time t', i.e. the slope of the function cannot be negative and positive for the forward and retract strokes, respectively. With $\mathrm{d}t'$ positive, the slope is positive in the forward stroke and negative in the retract stroke, i.e. from (2.3),

$$\left.\begin{aligned} &\mathrm{d}t' > 0 \\ &\therefore \frac{\mathrm{d}}{\mathrm{d}l'}(l' + \tfrac{1}{4}(\mathbb{T} - 1)\sin^2(2\pi l')) > 0 \end{aligned}\right\}, \tag{A1}$$

applying the derivative, the $\mathrm{d}t'$ results in

$$\mathrm{d}t' = 1 + \frac{\pi}{2}(\mathbb{T} - 1)\sin(4\pi l') > 0, \tag{A2}$$

now solving for $\mathbb{T}$,

$$(\mathbb{T} - 1)\sin(4\pi l') > -\frac{2}{\pi}. \tag{A3}$$

The $\sin(4\pi l')$ can be positive as well as negative, thus resulting in two set of inequalities given as

$$\mathbb{T} > 1 - \frac{2}{\pi \sin(4\pi l')} \quad \forall \sin(4\pi l') > 0, \tag{A4}$$

and

$$\mathbb{T} < 1 - \frac{2}{\pi \sin(4\pi l')} \quad \forall \sin(4\pi l') < 0. \tag{A5}$$

The right-hand sides of the inequality solutions ((A4) and (A5)) will maximize and minimize with the $\sin(4\pi l')$ value being maximum and minimum, respectively.

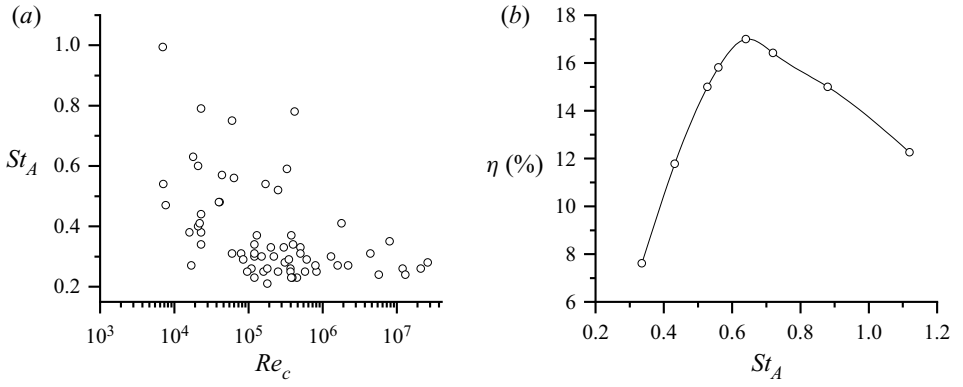

Figure 25. (*a*) Graph of St_A versus Re_c for different swimmers, data collected from various sources and tabulated by Eloy (2012). (*b*) Graph of η versus St_A for $\mathbb{T} = 1.00$.

The maximum and minimum values of the $\sin(4\pi l')$ are 1.0 and -1.0, respectively, which yields the limits $\mathbb{T} > 0.36$ and $\mathbb{T} < 1.64$, respectively. The solutions to the inequalities can also be seen visually in the contour plot of $\mathrm{d}t' > 0$ on the $l' - \mathbb{T}$ plane, as shown in figure 24(*b*). The dashed lines in figure 24(*b*) show the limits of $\mathbb{T} = (0.36, 1.64)$ within which $\mathrm{d}t' > 0$. It is worth noting that as the $\mathbb{T}$ approaches its limits, the time resolution to capture the flow would be very high because of extremely large velocities and other problems like cavitation, requiring excessively large C_P beyond the capacity of the fish or of an autonomous swimming robot.

A.2. *St_A for swimmers observed in Nature and the optimum efficiency*

The optimum St_A for swimmers and flyers observed in nature and reported in the literature is 0.2–0.4 (see e.g. Triantafyllou *et al.* 1993; Taylor *et al.* 2003). Figure 25(*a*) presents data collected by Eloy (2012) from over 40 different sources. It can be seen that as the Re_c becomes small, the St_A increases. The increase in St_A for low Re_c can be understood as the need for higher thrust to overcome the relatively larger viscous drag at low Re_c.

Figure 25(*b*) shows the dependence of η on St_A for $\mathbb{T} = 1.00$ at $Re_c = 10^3$. A maximum η of 17 % is achieved at $St_A = 0.63$ that is in the natural range of swimmers reported in the literature (figure 25*a*).

References

Akoz, E. & Moored, K.W. 2018 Unsteady propulsion by an intermittent swimming gait. *J. Fluid Mech.* **834**, 149–172.

Alam, M.M. & Muhammad, Z. 2020 Dynamics of flow around a pitching hydrofoil. *J. Fluids Struct.* **99**, 103151.

Andersen, A., Bohr, T., Schnipper, T. & Walther, J.H. 2016 Wake structure and thrust generation of a flapping foil in two-dimensional flow. *J. Fluid Mech.* **812**, R4.

Benkherouf, T., Mekadem, M., Oualli, H., Hanchi, S., Keirsbulck, L. & Labraga, L. 2011 Efficiency of an auto-propelled flapping airfoil. *J. Fluids Struct.* **27**, 552–566.

Berman, G.J. & Wang, Z.J. 2007 Energy-minimizing kinematics in hovering insect flight. *J. Fluid Mech.* **582**, 153–168.

Bohl, D.G. & Koochesfahani, M.M. 2009 MTV measurements of the vortical field in the wake of an airfoil oscillating at high reduced frequency. *J. Fluid Mech.* **620**, 63–88.

Chao, L.-M., Pan, G., Zhang, D. & Yan, G.-X. 2019 Numerical investigations on the force generation and wake structures of a nonsinusoidal pitching foil. *J. Fluids Struct.* **85**, 27–39.

CHILDRESS, S. 1981 *Mechanics of Swimming and Flying*. Cambridge University Press.
DAVID, M.J., GOVARDHAN, R.N. & ARAKERI, J.H. 2017 Thrust generation from pitching foils with flexible trailing edge flaps. *J. Fluid Mech.* **828**, 70–103.
DENG, J., SUN, L. & SHAO, X. 2015 Dynamical features of the wake behind a pitching foil. *Phys. Rev.* E **92**, 063013.
EGAN, B.C., BROWNELL, C.J. & MURRAY, M.M. 2016 Experimental assessment of performance characteristics for pitching flexible propulsors. *J. Fluids Struct.* **67**, 22–33.
ELOY, C. 2012 Optimal Strouhal number for swimming animals. *J. Fluids Struct.* **30**, 205–218.
FERNEX, D., SEMAAN, R., ALBERS, M., MEYSONNAT, P.S., SCHRÖDER, W. & NOACK, B.R. 2020 Actuation response model from sparse data for wall turbulence drag reduction. *Phys. Rev. Fluids* **5**, 073901.
FLORYAN, D., VAN BUREN, T., ROWLEY, C.W. & SMITS, A.J. 2017 Scaling the propulsive performance of heaving and pitching foils. *J. Fluid Mech.* **822**, 386–397.
GODOY-DIANA, R., AIDER, J.-L. & WESFREID, J.E. 2008 Transitions in the wake of a flapping foil. *Phys. Rev.* E **77**, 016308.
GODOY-DIANA, R., MARAIS, C., AIDER, J.-L. & WESFREID, J.E. 2009 A model for the symmetry breaking of the reverse Bénard–von Kármán vortex street produced by a flapping foil. *J. Fluid Mech.* **622**, 23–32.
HANCHI, S., BENKHEROUF, T., MEKADEM, M., OUALLI, H., KEIRSBULCK, L. & LABRAGA, L. 2013 Wake structure and aerodynamic characteristics of an auto-propelled pitching airfoil. *J. Fluids Struct.* **39**, 275–291.
HUERA-HUARTE, F.J. & GHARIB, M. 2017 On the effects of tip deflection in flapping propulsion. *J. Fluids Struct.* **71**, 217–233.
JAYNE, B.C., LOZADA, A.F. & LAUDER, G.V. 1996 Function of the dorsal fin in bluegill sunfish: motor patterns during four distinct locomotor behaviors. *J. Morphol.* **228**, 307–326.
VON KÁRMÁN, T. & BURGERS, J.M. 1934 General aerodynamic theory: perfect fluids. In *Aerodynamic Theory* (ed. W.F. Durand), vol II, Div. E, pp. 280–310. Springer-Verlag.
KATZSCHMANN, R.K., DELPRETO, J., MACCURDY, R. & RUS, D. 2018 Exploration of underwater life with an acoustically controlled soft robotic fish. *Sci. Robot.* **3**, eaar3449.
KE, X., ZHANG, W., CAI, X. & CHEN, W. 2017 Wing geometry and kinematic parameters optimization of flapping wing hovering flight for minimum energy. *Aerosp. Sci. Technol.* **64**, 192–203.
KOOCHESFAHANI, M.M. 1989 Vortical patterns in the wake of an oscillating airfoil. *AIAA J.* **27**, 1200–1205.
LU, K., XIE, Y.H. & ZHANG, D. 2013 Numerical study of large amplitude, nonsinusoidal motion and camber effects on pitching airfoil propulsion. *J. Fluids Struct.* **36**, 184–194.
MACKOWSKI, A.W. & WILLIAMSON, C.H.K. 2015 Direct measurement of thrust and efficiency of an airfoil undergoing pure pitching. *J. Fluid Mech.* **765**, 524–543.
MARAIS, C., THIRIA, B., WESFREID, J.E. & GODOY-DIANA, R. 2012 Stabilizing effect of flexibility in the wake of a flapping foil. *J. Fluid Mech.* **710**, 659–669.
MARTIN, N., ROH, C., IDREES, S. & GHARIB, M. 2017 To flap or not to flap: comparison between flapping and clapping propulsions. *J. Fluid Mech.* **822**, R5.
MORICHE, M., FLORES, O. & GARCÍA-VILLALBA, M. 2016 Three-dimensional instabilities in the wake of a flapping wing at low Reynolds number. *Intl J. Heat Fluid Flow* **62**, 44–55.
MURAYAMA, M. & YAMAMOTO, K. 2008 Comparison study of drag prediction by structured and unstructured mesh method. *J. Aircraft* **45**, 799–822.
MURAYAMA, M., YAMAMOTO, K. & KOBAYASHI, K. 2006 Validation of computations around high-lift configurations by structured- and unstructured-mesh. *J. Aircraft* **43**, 395–406.
RASPA, V., GODOY-DIANA, R. & THIRIA, B. 2013 Topology-induced effect in biomimetic propulsive wakes. *J. Fluid Mech.* **729**, 377–387.
SCHNIPPER, T., ANDERSEN, A. & BOHR, T. 2009 Vortex wakes of a flapping foil. *J. Fluid Mech.* **633**, 411–423.
SHADWICK, R.E. & LAUDER, G.V. 2006 *Fish Physiology: Fish Biomechanics*. Elsevier Science.
TAYLOR, G.K., NUDDS, R.L. & THOMAS, A.L.R. 2003 Flying and swimming animals cruise at a Strouhal number tuned for high power efficiency. *Nature* **425**, 707.
TIAN, W., BODLING, A., LIU, H., WU, J.C., HE, G. & HU, H. 2016 An experimental study of the effects of pitch-pivot-point location on the propulsion performance of a pitching airfoil. *J. Fluids Struct.* **60**, 130–142.
TRIANTAFYLLOU, M.S., HOVER, F.S., TECHET, A.H. & YUE, D.K. 2005 Review of hydrodynamic scaling laws in aquatic locomotion and fishlike swimming. *Appl. Mech. Rev.* **58**, 226–237.
TRIANTAFYLLOU, M.S., TRIANTAFYLLOU, G.S. & GOPALKRISHNAN, R. 1991 Wake mechanics for thrust generation in oscillating foils. *Phys. Fluids* A **3**, 2835–2837.
TRIANTAFYLLOU, G.S., TRIANTAFYLLOU, M.S. & GROSENBAUGH, M.A. 1993 Optimal thrust development in oscillating foils with application to fish propulsion. *J. Fluids Struct.* **7**, 205–224.

VAN BUREN, T., FLORYAN, D., WEI, N. & SMITS, A.J. 2018 Flow speed has little impact on propulsive characteristics of oscillating foils. *Phys. Rev. Fluids* **3**, 013103.

VIDELER, J.J. 1981 Swimming movements, body structure and propulsion in cod Gadus morhua. In *Symposia of the Zoological Society of London* 48, pp. 1–27.

WALD, R.M. 2010 *General Relativity*. University of Chicago press.

WANG, Q., GOOSEN, J.F.L. & KEULEN, F.V. 2017 Optimal pitching axis location of flapping wings for efficient hovering flight. *Bioinspir. Biomim.* **12**, 056001.

WHITE, F.M. 2003 *Fluid Mechanics*, 5th edn. McGraw-Hill.

XIAO, Q. & LIAO, W. 2009 Numerical study of asymmetric effect on a pitching foil. *Intl J. Mod. Phys.* C **20**, 1663–1680.

XIE, Y., LU, K., ZHANG, D. & XIE, G. 2014 Computational analysis of propulsion performance of modified pitching motion airfoils in laminar flow. *Math. Prob. Engng* **2014**, 1–13.

ZHANG, X., HE, G., WANG, S. & ZHANG, X. 2018 Locomotion of a bioinspired flyer powered by one pair of pitching foils. *Physical Review Fluids* **3**, 013102.